Unusual Tropical Cyclone Tracks under the Influence of Upper-Tropospheric Cold Low

HAN LI,[a] ZIYU YAN,[b,c] MELINDA PENG,[d] XUYANG GE,[a] AND ZHUO WANG[e]

[a] *Key Laboratory of Meteorological Disaster of Ministry of Education, Joint International Research Laboratory of Climate and Environment Change, Collaborative Innovation Center on Forecast and Evaluation of Meteorological Disasters, Nanjing University of Information Science and Technology, Nanjing, China*
[b] *State Key Laboratory of Severe Weather, Chinese Academy of Meteorological Sciences, Beijing, China*
[c] *School of Geo-Science and Technology, Zhengzhou University, Zhengzhou, China*
[d] *University of Colorado Colorado Springs, Colorado Springs, Colorado*
[e] *Department of Atmospheric Sciences, University of Illinois Urbana–Champaign, Urbana, Illinois*

(Manuscript received 4 April 2023, in final form 24 October 2023, accepted 26 October 2023)

ABSTRACT: Tropical cyclones (TCs) accompanied by an upper-tropospheric cold low (CL) can experience unusual tracks. Idealized simulations resembling observed scenarios are designed in this study to investigate the impacts of a CL on TC tracks. The sensitivity of the TC motion to its location relative to the CL is examined. The results show that a TC follows a counterclockwise semicircle track if initially located east of a CL, while a TC experiences a small southward-looping track, followed by a sudden northward turn if initially located west of a CL. A TC on the west side experiences opposing CL and β steering, while they act in the same direction when a TC is on the east side of CL. The steering flow analyses show that the steering vector is dominated by upper-level flow induced by the CL at an early stage. The influence of CL extends downward and contributes to the lower-tropospheric asymmetric flow pattern of TC. As these two systems approach, the TC divergent outflow erodes the CL. The CL circulation is deformed and eventually merged with the TC when they are close. Since the erosion of CL, the TC motion is primarily related to β gyres at a later stage. The sensitivity of TC motion to the CL depth is also examined. TCs located west of a CL experience a westward track if the CL is shallow. In contrast, TCs initially located east of a CL all take a smooth track irrespective of the CL depth, and the CL depth mainly influences the track curvature and the TC translation speed.

SIGNIFICANCE STATEMENT: The purpose of this study is to better understand how an upper-tropospheric cold low affects the motion of a nearby tropical cyclone. Our findings highlight distinct track patterns based on the relative positions of the tropical cyclone and the cold low. When the tropical cyclone is located on the east side of a cold low, a mutual rotation occurs, leading to a counterclockwise semicircle track of tropical cyclone. Conversely, if the tropical cyclone is located to the west side of a cold low, the cold low approaches and captures it, resulting in an abrupt northward turn when the cold low is eroded by the tropical cyclone. These insights improve the predictability of tropical cyclones in the vicinity of cold lows.

KEYWORDS: Cutoff lows; Storm tracks; Tropical cyclones

1. Introduction

Tropical cyclone (TC) motions are influenced by large-scale circulation (e.g., subtropical high pressure, monsoon trough, etc.) as well as the β effect (Holland 1983; Harr and Elsberry 1995; Lander 1996). TC tracks are usually westward or northwestward under the prevailing easterly flow at lower latitudes in the tropics before recurving poleward by the steering of nearby systems such as subtropical high pressure (Harr and Elsberry 1991, 1995; Lander 1996; Wu and Wang 2004; Camargo et al. 2007). TCs can also experience "unusual tracks," such as sharp turns or looping, as TCs interact with nearby synoptic or mesoscale systems and with other TCs (Carr and Elsberry 1995; Wu et al. 2011; Bi et al. 2015; Liang and Wu 2015; Ge et al. 2018; Liou and Pandey 2020; Yan et al. 2021).

Despite significant advances in forecasting TC tracks, predicting unusual tracks remains challenging (Qian et al. 2012, 2013). It is found that some mid- to lower-tropospheric systems can lead to sharp TC turns over the WNP (Lander and Holland 1993; Carr and Elsberry 1995, 1998; Bi et al. 2015; Liang and Wu 2015; Ge et al. 2018). For instance, the interaction between TC and a nearby monsoon gyre can lead to a sharp turning of a TC motion over WNP (Carr and Elsberry 1995; Bi et al. 2015; Liang and Wu 2015; Ge et al. 2018). Moreover, the interaction of two TCs, known as the Fujiwara effect, can also lead to unusual TC tracks (Lander and Holland 1993; Carr and Elsberry 1998; Bi et al. 2015). The above studies mainly focus on the mid- to lower-tropospheric systems impacting TC motions.

The influence of upper-tropospheric weather systems on TC motions has gained more attention recently. The upper-tropospheric cold low (CL) is a prominent weather system affecting TC tracks in the western North Pacific (WNP; Sadler 1975; Patla et al. 2009; Wei et al. 2016; Wen et al. 2019;

Corresponding author: Xuyang Ge, xuyang@nuist.edu.cn

DOI: 10.1175/MWR-D-23-0074.1

Ito et al. 2020; Yan et al. 2021). Wang et al. (2012) classified CLs into two categories based on their locations and movements: tropical upper-tropospheric trough (TUTT) cells and cutoff low types. Most CLs are generated out of the TUTT and move westward, known as TUTT cells (Palmer 1953; Sadler 1976). In contrast, cutoff lows originated from the midlatitude westerlies and tend to move eastward (Palmén 1949; Molinari and Vollaro 1989; Postel and Hitchman 1999). Chen and Ding (1979) suggested that the interaction between a CL and a TC is comparable to the Fujiwara interaction between two TCs. Patla et al. (2009) developed a conceptual model for TC–CL interactions and suggested that the relative distance, orientation, intensity, and size of the CL are critical characteristics in determining the impact of the CL on the TC track. Chen et al. (2002) found that a TC tends to stagnate, spin, or move southward when it is located in the southwest quadrant of a CL, while a TC experiences a sudden westward turn when it is located in the northeast quadrant of a CL. Li et al. (2012) found that a CL could trigger a sudden northward turn by altering the horizontal vorticity advection and the ambient vertical wind shear. Wei et al. (2016) suggested that TCs located on the eastern side of a CL tend to experience an abrupt left turn when their separation distance is within 5°. The ensemble analysis by Wen et al. (2019) suggested that track forecast is also sensitive to the CL vertical structure.

Previous studies (Patla et al. 2009; Li et al. 2012; Wen et al. 2019; Lei et al. 2020; Yan et al. 2021) have highlighted that the failure to simulate the TC–CL interaction can lead to significant TC track errors. Recently, Yan et al. (2021) found that the interaction between Typhoon Jongdari (2018) and a CL leads to Jongdari's semicircle track in its early stage using the piecewise potential vorticity (PV) technique. In light of these findings, this study aims to better understand unusual TC tracks under the influence of CLs through idealized numerical simulations. The environmental backgrounds of Typhoon Jongdari (2018) and another Typhoon Ken-Lola (1989), both were subjected to the influence of a nearby CL, serve as the basis of the study.

The structure of this paper is as follows. Section 2 provides an overview of Typhoon Jongdari (2018) and Ken-Lola (1989) with their unusual tracks. The analysis provides some observational basis for the idealized simulations. Section 3 describes the model configuration and the experiment design. Experiments with different TC positions relative to the CL center are examined in section 4, and the simulations with different CL depths are presented in section 5. The conclusion and discussion are given in section 6.

2. Analysis of two cases with a nearby CL

Typhoon Jongdari in 2018 and Ken-Lola in 1989 are selected to illustrate the impact of the CL on TC tracks. Figures 1a and 1b show the tracks of TC and CL for Jongdari and Ken-Lora, respectively. The TC tracks are obtained from the 6-hourly IBTrACS best track data (Knapp et al. 2010, 2018), and the CL tracks are determined by the 250-hPa cyclonic circulation center in ERA5 (Hersbach et al. 2020). The primary periods of interest are from 0000 UTC 27 July to 0000 UTC 1 August for Jongdari and from 0600 UTC 30 July to 1200 UTC 2 August for Ken-Lola (Figs. 1a,b).

Jongdari experienced two unusual TC tracks during the period of interest. At 0000 UTC 27 July, Jongdari was located approximately 800 km to the southeast of a nearby CL and exhibited a counterclockwise mutual rotation with the CL. At 1800 UTC 28 July, Jongdari made landfall in Japan and moved to the north-northwest quadrant of CL, with a separation distance of 550 km at 0000 UTC 29 July. After moving off Japan, the CL and Jongdari merged at 1800 UTC 30 July. Thereafter, the movement of Jongdari changed from eastward to northwestward, resulting in a small loop motion between 30 July and 1 August (Fig. 1a).

Ken-Lola developed as a tropical depression at 0000 UTC 28 July 1989. At 0600 UTC 30 July, it was situated roughly 450 km to the southeast quadrant of a CL. Thereafter, the two systems rotated mutually when Ken-Lola experienced a large cyclonic semicircle track from 30 to 31 July similar to Jongdari. Ken-Lola was located northwest of CL at 1200 UTC 31 July, and these two entities eventually merged on 1 August. At its later stage, Ken-Lola experienced a northward turn from 1800 UTC 31 July to 1200 UTC 2 August (Fig. 1b).

The above analysis suggests that the unusual tracks of Jongdari and Ken-Lola may be related to a nearby CL and their relative positions to the CL may be important in determining the characteristics of the tracks. Furthermore, it is possible that TC tracks are sensitive to the vertical structure of the CL. Figures 1c and 1d compare the longitude–height cross sections of the meridional wind and temperature anomalies of the CLs in the Jongdari and Ken-Lola cases. The maximum cold core of the CL in the Jongdari case was located near 400 hPa. The circulation had a deep structure and extended downward to near the boundary layer (Fig. 1c). In contrast, the cold core of the CL in the Ken-Lola case peaked at 250 hPa, and its circulation was largely confined above 500 hPa (Fig. 1d). The different depths of the CLs may contribute to the different track behaviors of Jongdari and Ken-Lola. Idealized simulations are thus conducted to investigate the sensitivity of TC track to the relative location of the TC to the CL and the vertical extent of the CL.

3. Methodology and experiment designs

a. Model and experimental designs

The Advanced Research Weather Research and Forecasting (WRF-ARW) Model (version 3.9.1; Skamarock et al. 2008) is used to study the effects of the CL on TC track in an idealized framework. The model is configured with three two-way nested domains with horizontal resolutions of 27, 9, and 3 km, respectively. The outer domain covers an area of 6480 km × 6480 km centered at 25°N. The middle and innermost domains are of 1620 km × 1620 km and 540 km × 540 km, respectively. The two inner domains move with the storm during the integration. The model has 41 levels in the vertical. All experiments are integrated to 72 h on a β-plane, and based on 25°N.

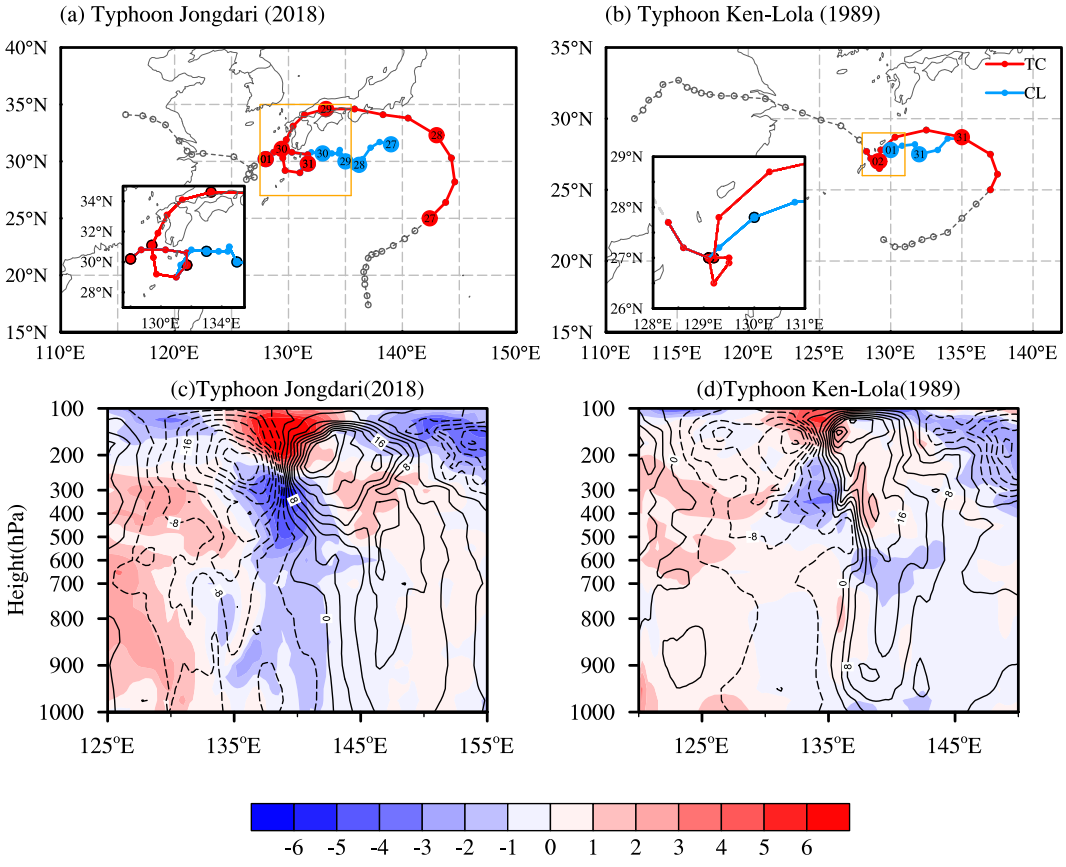

FIG. 1. (a),(b) The 6-hourly tracks (gray dashed line) of (a) Jongdari and (b) Ken-Lola. The solid line represents the period of interest in this study. The red (blue) solid lines represent the tracks of TC (CL). The inset is the zoomed-in area of the orange square box in (a) and (b). (c),(d) The longitude–height cross sections of the meridional wind (contours; unit: m s^{-1}; at 4 m s^{-1} intervals), temperature anomalies (shading; unit: K) near the CL at (c) 0000 UTC 27 Jul 2018 along 31.5°N and (d) 0600 UTC 30 Jul 1989 along 28.5°N. The temperature anomalies are defined with respect to the average over 100°–160°E.

The following physics parameterizations are used: the WRF single-moment 6-class (WSM6; Hong et al. 2010) microphysics scheme, the Dudhia (1989) shortwave radiation scheme, the Rapid Radiative Transfer Model (RRTM; Mlawer et al. 1997) longwave radiation scheme, the Yonsei University planetary boundary layer (PBL) scheme (Hong et al. 2006), and a modified MM5 surface layer scheme (Jiménez et al. 2012). The Kain–Fritsch convective scheme (Kain and Fritsch 1993) is only applied to the outmost domain.

The background flow is set to zero in all experiments. The tangential wind profile of the initial TC is given by Eq. (1):

$$V_t = \begin{cases} V_m \times \dfrac{r}{r_m} \times \sin\left(\dfrac{\pi}{2} \times \dfrac{\sigma - 0.1}{1 - 0.1}\right), & r \le r_m, \\ \left[V_m \times \left(\dfrac{r}{r_m}\right)^{(-0.75)} - V_{\mathrm{m}} \times \left(\dfrac{r_0}{r_m}\right)^{(-0.75)} \times \left|\dfrac{r - r_m}{r - r_0}\right|\right] \times \sin\left(\dfrac{\pi}{2} \times \dfrac{\sigma - 0.1}{1 - 0.1}\right), & r_m < r < r_0, \\ 0, & r > r_0, \end{cases} \tag{1}$$

where V_t is tangential wind, r is the radius, V_m is maximum tangential wind, r_m is the radius of V_m, σ is the model sigma level, and r_0 represents the radius where tangential wind equals 0 m s^{-1}. The TC vortex is initialized with a maximum tangential wind of 25 m s^{-1} at a radius of 75 km, and its strength decreases with height and to zero at 100 hPa.

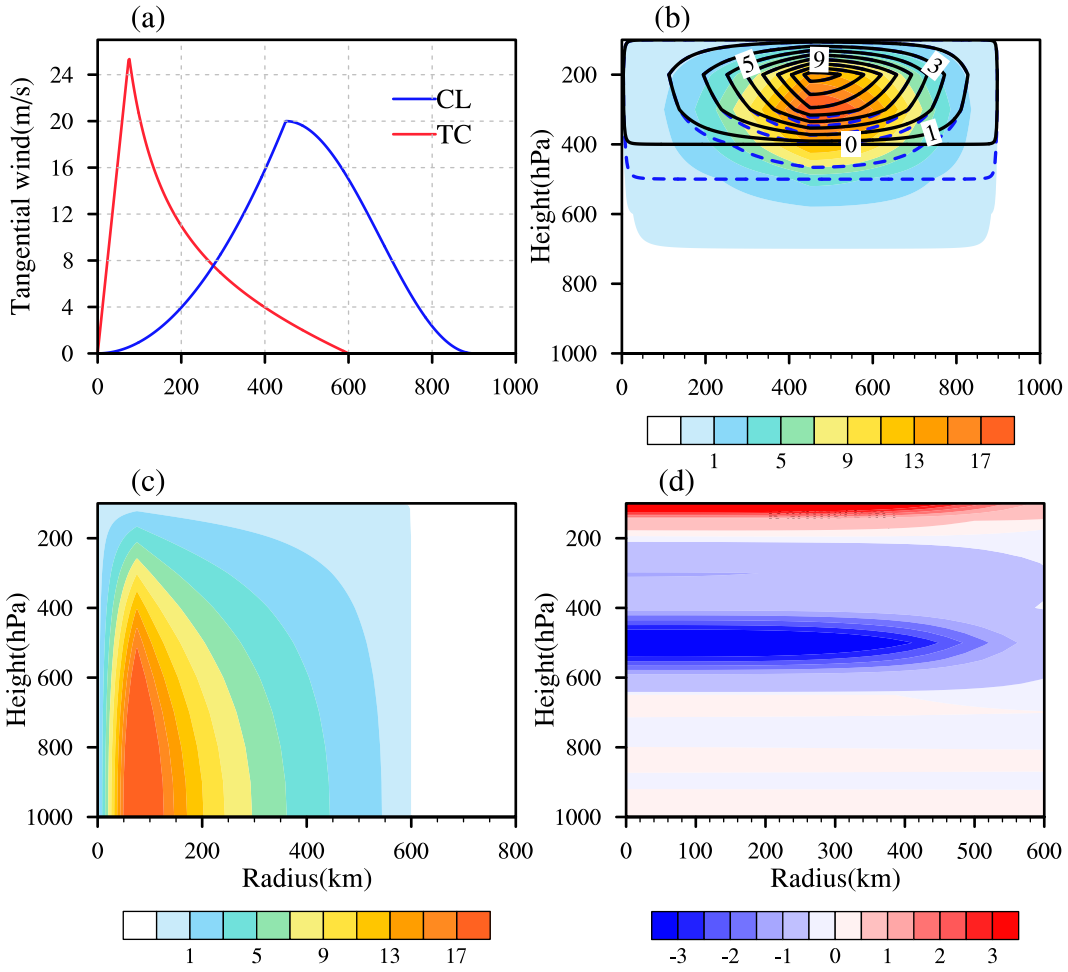

FIG. 2. (a) Initial radial profiles of tangential wind (unit: m s^{-1}) near the surface for the TC (red solid line) and at 250 hPa for the CL (blue solid line). (b) Vertical cross section of the tangential wind for the CL in Deep (shading), Medium (blue dashed contours), and Shallow (black solid contours) experiments. The contour intervals of the Medium and Shallow CL are the same as that of the deep CL. (c) Vertical cross section of the tangential wind for the TC (shading; unit: m s^{-1}). (d) Vertical cross section of the temperature anomaly (shading; unit: K) for the medium CL.

The tangential wind profile of initial CL is given by Eq. (2):

$$V_t = \begin{cases} V_m \times \dfrac{r^2}{r_m^2} \times a_m, & r \le r_m, \\ \dfrac{V_m}{2} \times \left[1 - \cos\left(\dfrac{\pi r}{r_m}\right)\right] \times a_m, & r_m < r \le 2r_m, \\ 0, & r > 2r_m. \end{cases} \tag{2}$$

The height variation coefficient a_m is given by Eq. (3):

$$a_m = \begin{cases} 0, & \sigma \le 0.1, \\ \cos\left[\dfrac{\pi}{2} \times (\sigma - \sigma_t)\right]^8, & 0.1 < \sigma \le 0.2, \\ \cos\left[\dfrac{\pi}{2} \times (\sigma - \sigma_t)\right]^2, & 0.2 < \sigma \le 0.4, \\ \cos\left[\dfrac{\pi}{2} \times (\sigma - \sigma_t)\right]^8, & 0.4 < \sigma \le \sigma_d, \\ 0, & \sigma > \sigma_d, \end{cases} \tag{3}$$

where σ_t is the height where the tangential wind of the CL reaches its maximum, and σ_d specifies the depth of the CL. The idealized CL has an initial maximum tangential wind of 20 m s^{-1} at the radius of 450 km at the upper level, similar to the structure of CL near Jongdari.

The initial radial profiles of tangential wind for the idealized TC and the CL are shown in Fig. 2a. The vertical structure of the CL and the TC are shown in Figs. 2b and 2c, with the zero tangential wind contour extending down to 700, 500, and 400 hPa for Deep, Medium, and Shallow CL, respectively (Fig. 2b). The structure of the "Deep" CL is to mimic the CL associated with Jongdari, with the maximum wind 20 m s^{-1} located at 300 hPa. The structure of the CL in the "Medium" and "Shallow" experiments resembles the structure of the CL associated with Ken-Lola, with the maximum tangential wind of 16 m s^{-1} at 200 hPa. The vertical profiles of the environmental temperature and moisture are based on the mean tropical sounding (Jordan 1958). By specifying these variables, the

geopotential height can be obtained by solving a nonlinear balanced equation (Wang 1995). The CL has a cold-core structure due to the thermal wind balance. Figure 2d shows the cold core of the medium CL as an example.

Thirteen experiments are set up to investigate the sensitivity of the TC track to its relative position to a nearby CL and the depth of the CL (Table 1). "In" indicates that the TC is located within the radius of maximum wind (RMW) of the CL initially, while "Out" indicates the TC is outside of the CL RMW. "Deep," "Medium," and "Shallow" represent CLs of different depths shown in Fig. 2b. The CL is excluded in the "noCL" experiment for the comparison with other experiments to show, in general, the role of CL on the TC motion. "SE" and "NW" indicate that the TC is initially located in the southeast and northwest quadrant of the CL, respectively. For reference, the setting of SE_Out_Deep is similar to Jongdari, whereas SE_Out_Medium is akin to Ken-Lola. We have also conducted NE and SW experiments. In general, the results of the SW experiments are similar to those of the SE experiments, while the NE experiments are similar to the NW experiments (not shown). Thus, since the idealized experiments are based on the real-world cases of Jongdari and Ken-Lola, we focus only on the NW and SE experiments in this paper.

TABLE 1. Summary of the idealized experiments.

Experiment	CL depth (hPa)	Initial distance of TC from CL's center (km)	The quadrant where the initial TC is located
NW_In_Deep	700	300	NW
NW_In_Medium	500	300	NW
NW_In_Shallow	400	300	NW
NW_Out_Deep	700	800	NW
NW_Out_Medium	500	800	NW
NW_Out_Shallow	400	800	NW
SE_In_Deep	700	300	SE
SE_In_Medium	500	300	SE
SE_In_Shallow	400	300	SE
SE_Out_Deep	700	800	SE
SE_Out_Medium	500	800	SE
SE_Out_Shallow	400	800	SE
noCL	—	—	—

b. PV–ω inversion

The outflow of a TC is an important aspect of its secondary circulation and can directly interact with the environment wind. Previous studies demonstrated that the divergent outflow associated with deep convections can alter the environmental flow around the TC (Ryglicki et al. 2019; Huang et al. 2022). Wang and Zhang (2003) developed a quasi-balanced PV–ω inversion system to diagnose the TC secondary circulation in response to external forcing. To quantify the CL–TC interaction, the quasi-balanced PV–ω inversion technique (Wang and Zhang 2003) is applied:

$$\nabla_h^2\left(\frac{\partial^2\Phi}{\partial z^2}\omega\right)+f\eta\frac{\partial}{\partial z}\left\{(z_a-z)^{-\mu}\frac{\partial}{\partial z}[(z_a-z)^{\mu}\omega]\right\}$$
$$-f\frac{\partial}{\partial z}\left(\frac{\partial\omega}{\partial x}\frac{\partial^2\Psi}{\partial x\partial z}+\frac{\partial\omega}{\partial y}\frac{\partial^2\Psi}{\partial y\partial z}\right)-f\frac{\partial}{\partial z}\left(\frac{\partial\omega}{\partial x}\frac{\partial^2\chi}{\partial y\partial z}-\frac{\partial\omega}{\partial y}\frac{\partial^2\chi}{\partial x\partial z}\right)$$
$$-\left(f\frac{\partial\eta}{\partial z}\frac{\mu}{z_a-z}+f\frac{\partial^2\eta}{\partial z^2}\right)\omega$$
$$=f\frac{\partial}{\partial z}(V_h\cdot\nabla\eta)-\nabla_h^2\left(V_h\cdot\nabla_h\frac{\partial\Phi}{\partial z}\right)-2\frac{\partial^2}{\partial t\partial z}\left[\frac{\partial^2\Psi}{\partial x^2}\frac{\partial^2\Psi}{\partial y^2}-\left(\frac{\partial^2\Psi}{\partial x\partial y}\right)^2\right]$$
$$-\beta\frac{\partial^3\Psi}{\partial t\partial y\partial z}+\frac{g}{\theta_0}\nabla_h^2\dot{q}_p-f\frac{\partial}{\partial z}\left(\frac{\partial f_y}{\partial x}-\frac{\partial f_x}{\partial y}\right)-\frac{\partial^2}{\partial t\partial z}\left(\frac{\partial f_x}{\partial x}-\frac{\partial f_y}{\partial y}\right), \tag{4}$$

$$\nabla_h^2\chi=-(z_a-z)^{-\mu}\frac{\partial}{\partial\hat{z}}[(z_a-z)^{\mu}\omega], \tag{5}$$

where $\mu = c_v/R_d$, $V_h = V_\Psi + V_\chi$, Ψ and χ are the total streamfunction and velocity potential; Φ, η, and ω are the geopotential height, absolute vorticity, and vertical velocity; f_x and f_y are the latitudinal and meridional friction, respectively; $z = (1 - \pi/C_p)z_a$ is the pseudo-height coordinate; $z_a = (C_p/R_d)H_s$; $H_s = p_0/\rho_0 g = R_d\theta_0/g$ is the scale height; Θ_0 is the reference potential temperature; p_0 is the surface pressure; and $\dot{q}_p$ is the diabatic heating. In Eq. (4), the first four terms are the dynamic forcings, whereas the last three terms are the thermodynamical forcings. The thermodynamical forcing primarily refers to the latent heating, mainly attributed to moist convections in the eyewall and spiral rainbands. In this study, the relative contribution of the thermodynamic forcing to the TC outflow will be examined.

c. PV tendency budget

Previous studies have shown that TCs usually move toward the maximum of the azimuthal wavenumber one component of the PV tendency (Holland 1983; Shapiro and Franklin 1995; Wu and Kurihara 1996; Wu and Wang 2000; Chan et al. 2002; Bi et al. 2015). The PV tendency equation (Wu and Wang 2000) in isobaric coordinates, as expressed below, is used to diagnose TC motion:

$$\frac{\partial P}{\partial t}=\mathrm{HAD}+\mathrm{VAD}+\mathrm{DHT}+F_*, \tag{6}$$

$$\mathrm{HAD}=-u\frac{\partial P}{\partial x}-v\frac{\partial P}{\partial y}, \tag{7}$$

$$\mathrm{VAD}=-\omega\frac{\partial P}{\partial p}, \tag{8}$$

$$\mathrm{DHT}=-g\left[(\zeta+f)\frac{\partial Q}{\partial p}+\frac{\partial Q}{\partial y}\frac{\partial u}{\partial p}-\frac{\partial Q}{\partial x}\frac{\partial v}{\partial p}\right], \tag{9}$$

where P is the PV in the pressure coordinates; u, v, and ω are the zonal wind, meridional wind, and vertical velocity; ζ and f are the relative vorticity and Coriolis parameter; $Q = Q_1/(C_p\pi)$, where $\pi = (p/100\,000)^{R/C_p}$, and Q_1 is the total diabatic heating rate and can be obtained from the model simulation. In Eq. (6), the first term on the left side is the local PV tendency (PVT), while the right side includes the horizontal advection of the

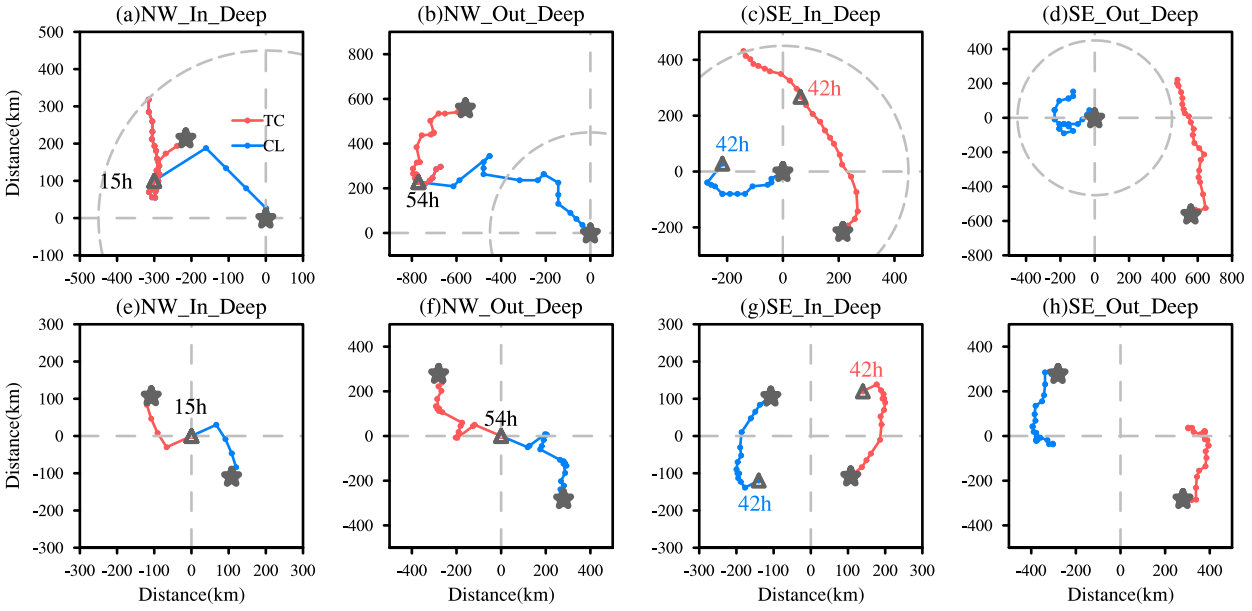

FIG. 3. (a)–(d) The 3-hourly tracks of TC (red lines) and CL (blue lines) relative to the initial CL center (0, 0). (e)–(h) The relative positions between TC and CL with (0, 0) being the middle point between them at each time. The gray stars denote the initial positions of TC and CL, and the gray triangles represent their positions when the CL has dissipated or merged with the TC.

potential vorticity (HAD), the vertical advection of the potential vorticity (VAD), the PV tendency associated with the diabatic heating (DHT) and friction (F_*).

4. TC motions with different initial positions relative to the CL

a. *Simulated tracks*

In this section, we examine the influence of the CL on the TC motion when the TC is located initially at different positions relative to the CL center. We first focus on the "Deep" simulations as they possess strongest interactions between the CL and the TC. The "Medium" and "Shallow" experiments will be discussed in section 5. The tracks and relative positions of TC and CL in the four experiments with the same deep CL but different initial positions relative to the CL center are displayed in Fig. 3. The CL center is determined by analyzing the 400-hPa cyclonic circulation. The TC center is determined based on the location of the minimum sea level pressure. As the CL initially steers the TC, the different TC–CL orientations result in varying initial TC movement directions. When the TC is initially located on the west side of the CL center, it experiences a small looping track followed by a sudden northward turn (Figs. 3a,b,e,f). If it is initially located to the east of the CL, it has a cyclonic semicircle track (Figs. 3c,d,g,h).

In the "NW" experiments, the CL moves northwestward toward the TC (Figs. 3a,b). The two entities engage in a mutually rotating counterclockwise motion while approaching each other, and eventually merge (Figs. 3e,f). Similar to the Fujiwara effect between two TCs. The direction of the TC motion in NW_In_Deep changes abruptly at T = 27 h from southwestward to northeastward, while the TC turns at T = 54 h in the NW_Out_Deep. Both experiments show a decrease in the TC speed near the turning point, with the moving speed in NW_Out_Deep dropping more sharply. In NW_In_Deep, the CL merges with the TC at T = 15 h, after which the translation speed of TC slows down significantly. In NW_Out_Deep, the TC turns northeastward soon after the merger at T = 54 h. In this study, the merging is defined as when the CL and TC centers are within 200 km of each other.

In contrast, TCs in the "SE" experiments take a larger-scale cyclonic semicircle track. The CL moves westward while the TC moves northeastward in the first few hours (Figs. 3c,d), and they show a tendency to drift away from each other (Figs. 3g,h). In SE_In_Deep, the TC motion changes from northeastward to northwestward during T = 0–18 h. The separation distance between CL and TC increases during this period. After T = 24 h, their separation distance remains around 450 km, and the CL dissipates by T = 42 h. In SE_Out_Deep, the distance between TC and CL fluctuates around 800 km. At T = 36 h, the separation distance between the TC and CL is reduced to 600 km by T = 72 h. In the "SE" experiments, the TC and CL mainly exhibit mutual rotation without merging (Figs. 3g,h). We tested different initial separation distances between 100 and 800 km, and the results are consistent with those shown in Fig. 3. In short, a TC east of a CL moves in a cyclonic semicircle track by the steering of the CL circulation, while a TC west of a CL moves southward initially also steered by the CL anticyclonic circulation but it would experience an abrupt northward turn at a later stage. Distinctive differences also occur between when the TC is in and out of the RMW of the CL as shown in Fig. 3. We will discuss the dynamics behind these differences in more detail in the following section.

b. Interactions between TC and CL

PV is a useful parameter for understanding the TC–CL interaction (Wu and Emanuel 1995a,b; Shapiro 1996; Shapiro and Franklin 1999; Wu and Kurihara 1996; Wu and Wang 2000; Hanley et al. 2001; Chan et al. 2002) and is examined in this section. Figures 4 and 5 present the evolution of the 400-hPa PV and wind fields and the cross sections of PV along the TC and the CL centers in NW_In_Deep and NW_Out_Deep (Fig. 4) and SE_In_Deep and SE_Out_Deep (Fig. 5).

Since the CL has a larger size than the TC at the upper level (Figs. 4a,g), it has a larger β-induced westward propagation speed, ultimately catching up with the TC in the "NW" experiments (Figs. 3a,b). In NW_In_Deep, as two entities rotate and approach each other, the structure of the CL is distorted due to their close proximity (Figs. 3e and 4a–c). Since the TC is initially located within the RMW of CL, their PV towers partially overlap (Fig. 4a). By $T = 18$ h, the circular PV structure of the CL is stretched into a thin strip (Fig. 4b). As the filamented PV of the CL merges into the large PV of TC in the middle to upper levels (Fig. 4f), TC takes a northward track when the steering from the CL diminished (Figs. 3a and 4c). The TC–CL interaction displays distinct characteristics above and below the 300 hPa (Fig. 4f). Below 300 hPa, the residual PV of the CL is deformed into spiral PV bands wrapping around the TC, accompanied by an increase in the TC scale at $T = 42$ h (Fig. 4c). However, the PV column above 300 hPa moves away from the TC, and the structure of CL is gradually eroded (Fig. 4f).

Due to their larger initial distance between TC and CL in NW_Out_Deep, the approach rate between the TC and the CL is slower compared with that in NW_In_Deep. In the beginning, an elastic interaction occurs between the CL and the TC (Fig. 4g). That is, CL and TC only distort slightly without significant changes in their structure and intensity (Dritschel and Waugh 1992; Khain et al. 2000). The western side of the CL circulation deforms further with time (Figs. 4g,h). Below 300 hPa, the PV column of the CL approaches and connects with that of TC, and its magnitude gradually weakens during $T = 6$–18 h (Figs. 4j,k), similar to that of NW_In_Deep (Figs. 4d,e). At $T = 42$ h, some PV filaments of the CL approach and merge with the TC, resulting in a decrease of the TC's translation speed (Figs. 3b and 4i,l). Above 300 hPa, the PV remnants of the CL move away from the TC (Figs. 4k,l), similar to NW_In_Deep (Figs. 4e,f).

In SE_In_Deep, the TC initially moves with the steering from the CL circulation (Fig. 3c), and TC and CL rotate around each other (Fig. 3g). The large separation distance helps to maintain the CL circulation, and the PV deformation is weaker than those counterparts in the "NW" experiments (Figs. 4c and 5c). The approaching rate between TC and CL is slower in SE_In_Deep than in NW_In_Deep as both the β steering and the steering by the CL circulation move roughly in the same north-by-northwest direction (Figs. 3e,g). Likewise, in SE_Out_Deep, the deformation of CL is weaker than that in NW_Out_Deep, since the separation distance remains greater than 700 km (Figs. 3d, 4g–i, and 5g–i). The CL structure remains distinct at $T = 42$ h in the "SE" experiments (Figs. 5c,i), indicating a weaker TC–CL interaction.

The TC–CL interaction bears many similarities with the binary TC interaction described by Kuo et al. (2004), although the TC and the CL circulations peak at different heights. In particular, when the CL and the TC are far apart, there is an elastic interaction (Figs. 4g and 5g). Once the two entities move closer, the CL will be stretched into PV filaments surrounding the TC (Figs. 4b,c and 5b,c), similar to the behavior of the weaker TC in the binary TC interaction.

To further investigate the underlying mechanisms, the quasi-balanced PV–ω inversion technique is applied to quantify the TC–CL interaction (see section 3b). This method computes the divergent flow forced by the diabatic heating (Wang and Zhang 2003). Since the CL is generally observed as a clear-sky region with a weak downward motion (Kelley and Mock 1982; Chen and Chou 1994; Patla et al. 2009; Wen et al. 2018), the divergent outflow in the upper troposphere is largely driven by the diabatic forcing associated with the TC. Hence, we derive the divergent wind forced by the diabatic heating of the TC to investigate the role of TC upper-level divergent flows in affecting the CL circulation.

Figure 6 displays the distribution of the divergent wind, the diabatic heating, and the PV field at 14-km height at $T = 33$ h in our four major experiments. In NW_In_Deep, the maximum of upper-level averaged diabatic heating (black contours) can reach up to 1.1 K h^{-1} and extend up to 200 km from the TC center. In contrast, the maximum of averaged diabatic heating in SE_In_Deep is only 0.6 K h^{-1} and is confined within 100 km of the TC center. The greater and wider diabatic heating in NW_In_Deep thus induces stronger and wider divergent winds than in SE_In_Deep (Figs. 6a,c). As a result, under the Coriolis force, the upper-level divergent outflow will form an anticyclonic component, which ultimately erodes the CL, especially when CL and TC are in close proximity (Figs. 6e,g). Since the TC outflow is mainly above 300 hPa, the CL circulation is susceptible to a rapid decay therein. In contrast, the CL circulation below 300 hPa can persist for a longer time. This outflow erosion process is highly sensitive to the TC position, and the impact is greater when TC is located closer to the CL center (Figs. 6e–h). For instance, although the TC divergent outflow is strong due to the strong diabatic heating of TC (Fig. 6b), the larger separation distance between the TC and the CL is the reason for the slower erosion rate of the CL compared to NW_In_Deep (Figs. 6e,f).

c. Steering flow

It has been well realized that the TC motion is largely determined by the steering flow of its environment (Chan and Gray 1982; Velden and Leslie 1991; Galarneau and Davis 2013). The top of each panel in Fig. 7 presents the evolution of the steering vectors between 850 and 200 hPa by the mean flow averaged within a radius of 600 km following the TC center in the four experiments. The bottom of each panel in Fig. 7 includes the movement vector of the TC (red arrows at the bottom) and the total steering flow (black arrows at the bottom). The total steering flow is determined by the vertical average of the steering vectors at each level between 850 and 200 hPa for the "NW" experiments and between 850 and

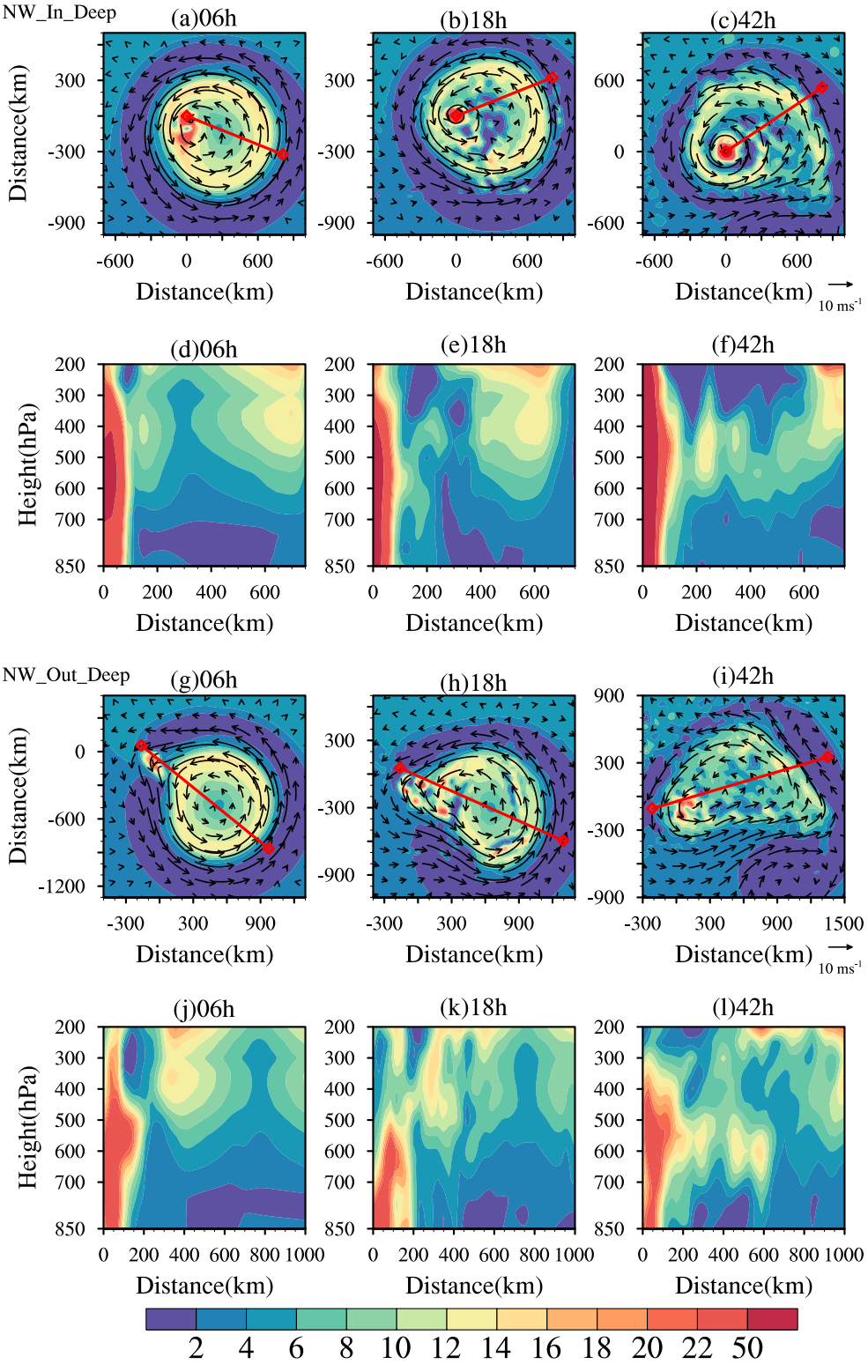

FIG. 4. (a)–(c) Evolutions of 400-hPa potential vorticity (shading; units: 0.1 PVU) and wind field (vectors; unit: m s^{-1}). (d)–(f) The oblique cross sections of potential vorticity along the TC and the CL center in NW_In_Deep. (g)–(l) As in (a)–(f), but for NW_Out_Deep, all from T = 6–42 h. The point (0, 0) in the horizontal plane is the TC center and the red solid line indicates the position where the cross section is taken.

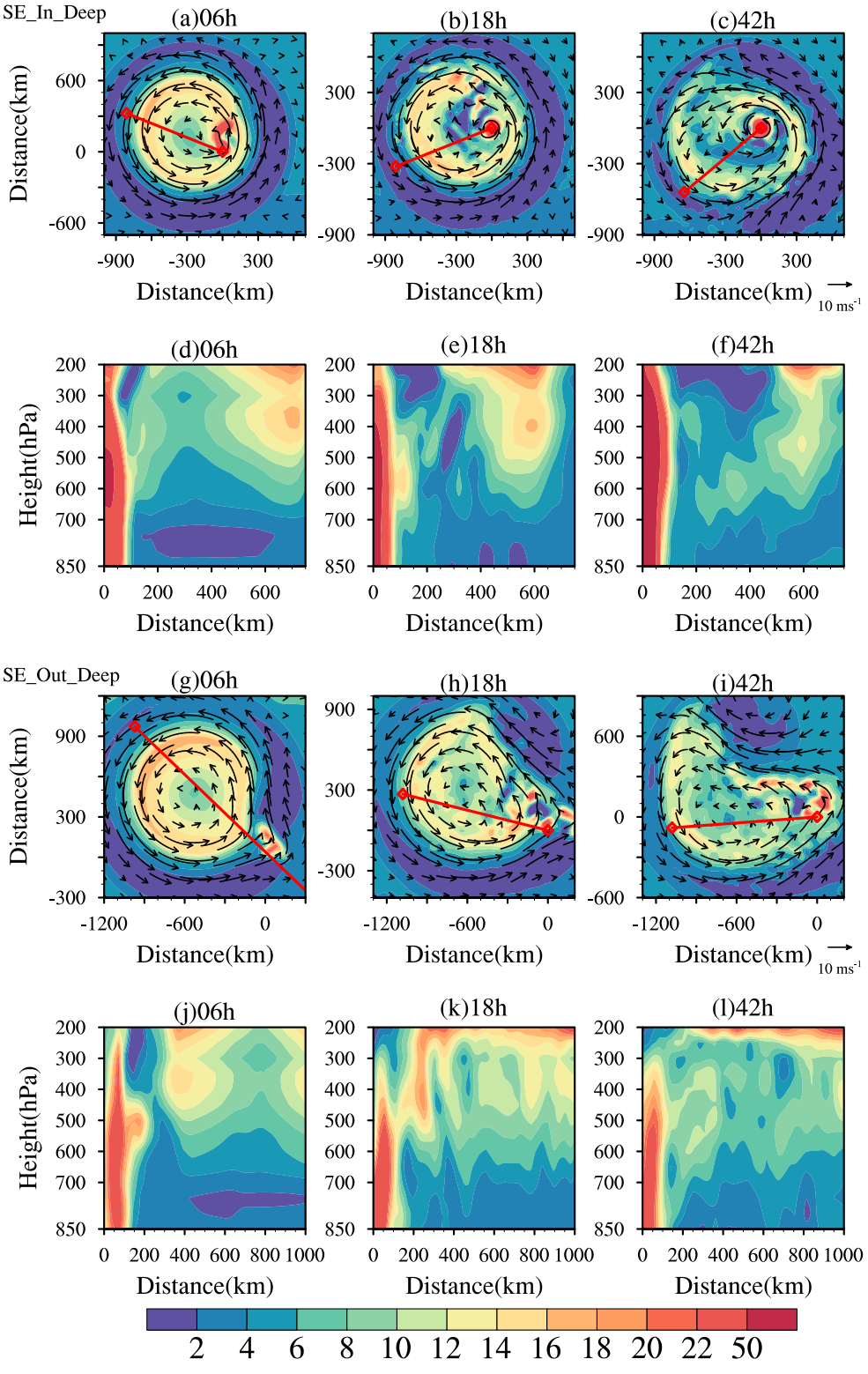

FIG. 5. As in Fig. 4, but for (a)–(f) SE_In_Deep and (g)–(l) SE_Out_Deep.

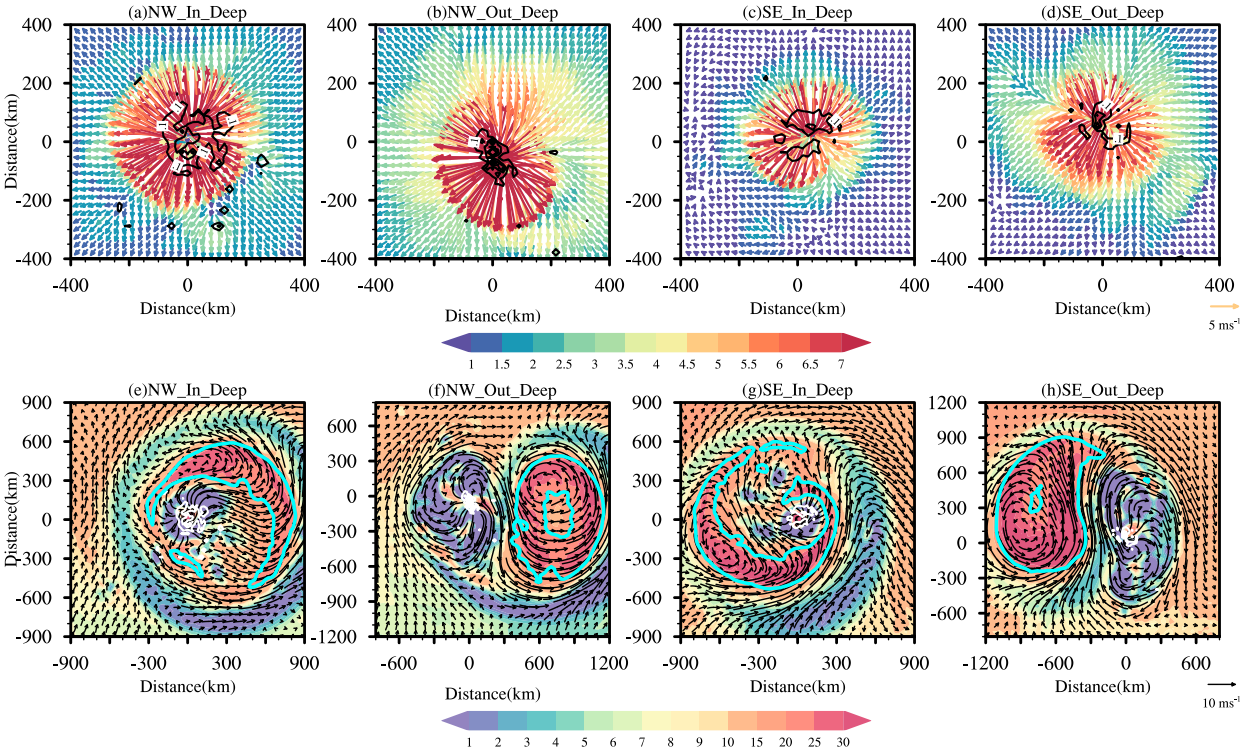

FIG. 6. (a)–(d) The 14-km divergent wind (vectors; units: m s^{-1}) and the 13–15-km vertically averaged diabatic heating (black contours at 0.1, 0.6, 1.1, 1.6, 2.1 K h^{-1}; units: K h^{-1}) at T = 33 h. (e)–(h) The 14-km total wind (vectors; units: m s^{-1}), the potential vorticity (shading; units: 0.1 PVU), and the diabatic heating (white contours at 0.1, 0.6, 1.1, 1.6, 2.1 K h^{-1}; units: K h^{-1}) at T = 33 h. The point (0, 0) is the TC center, and the thicker cyan contours in (e)–(h) denote the large PV of the CL defined as the PV larger than 2 PVU.

350 hPa for the "SE" experiments. The determination of steering flows follows the methodology introduced by Galarneau and Davis (2013). With mean deviations all less than 1.5 m s^{-1}, the vertical averaged total steering vectors (black arrows at the bottom) well represent the TC motions in all simulations. The strong upper-tropospheric steering flow driven by the CL circulation has a larger contribution to the total steering flow in the early stage in all simulations (Fig. 7). With the erosion of the CL (Figs. 4–6), the upper-tropospheric steering flow (above 550 hPa) decreases and the lower-tropospheric steering flow (below 550 hPa) increases at the later stage in most experiments. The increasing contribution of the lower-level flow to the total steering flow results in the shift of TC motion vector, especially in the "NW" experiments (Figs. 7a,b). This transition of the steering flow contributions from different layers was also found in the steering flows of TC Rex2 (1998) by Patla et al. (2009) and Jongdari (2018) by Yan et al. (2021).

To quantitatively compare the evolution of the steering flow, Fig. 8 presents the temporal evolution of the upper-tropospheric steering flow, lower-tropospheric steering flow, and the total steering flow in four "Deep" experiments. The upper-tropospheric and lower-tropospheric steering flow is defined as the height-averaged steering flow above and below 550 hPa, respectively. In NW_In_Deep, the upper-tropospheric steering flow contributes more to the TC movement at the early stage (T = 0–24 h). Since the CL is mainly confined above 700 hPa initially, the associated upper-tropospheric steering flow is southward and cyclonic in this experiment (Figs. 8a,e). During 18–36 h (Fig. 3a), the CL structure is rapidly eroded as it approaches the TC (Figs. 4b,c,e,f). The upper-tropospheric steering flow thus weakens and changes from northeasterly to southwesterly flow. More specifically, the southeasterly flow at the lower tropospheric strengthens and counters the southwesterly flow at the upper-tropospheric after T = 24 h. The zonal component of the upper-tropospheric and lower-tropospheric steering flows are opposite during T = 24–72 h. Accompanying this change, there is a shift in the TC motion vector from northeastward to northward (Figs. 8a,e). In NW_Out_Deep, the meridional component of lower-tropospheric steering flow provides a larger contribution to the total steering flow after T = 54 h (Fig. 8f). The lower-tropospheric steering gradually increases, together with the weakening of the upper-tropospheric steering flow, causing a small looping track after T = 54 h (Fig. 5).

In SE_In_Deep, the upper-tropospheric steering flow contributes more to the total steering flow during T = 0–42 h (Figs. 8c,g) due to the longer persistence of the CL (Figs. 3a,c). As a result, the TC moves northeastward and northwestward following the circulation of the CL. The upper-tropospheric steering flow gradually diminishes as the CL circulation decays, and the contribution of lower-tropospheric steering flow enhances after T = 42 h (Figs. 5b,c and 8c,g). The meridional component of lower-tropospheric steering flow exceeds that of

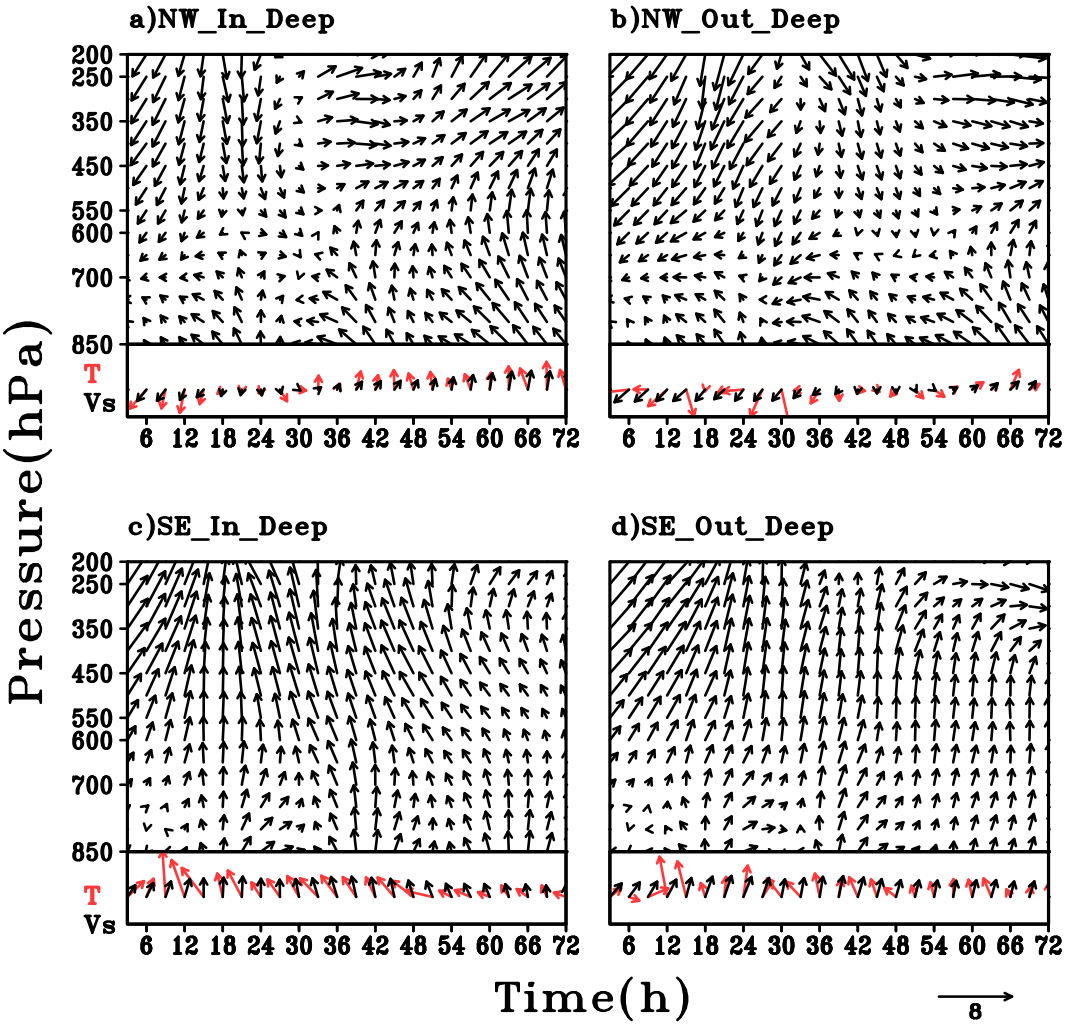

FIG. 7. (top) The time–height profiles of the steering flow (unit: m s^{-1}) averaged within a 600 km × 600 km box following the TC center. (bottom) The evolutions of optimal steering flow for each experiment. At the bottom of the figure, "T" denotes the TC movement (red vectors), and "Vs" denotes the total steering flow (black vectors).

the upper-tropospheric steering flow after $T = 60$ h (Fig. 8g). This lower-tropospheric steering flow mainly comes from the β-steering and it will be discussed further in section 4e. The variations of the TC track and steering flow during this stage are similar to the real-case study of Jongdari by Yan et al. (2021). In SE_Out_Deep, the steering vector is mainly influenced by the steering at the upper levels above 550 hPa before $T = 24$ h, and the upper and lower tropospheric make comparable contributions afterward (Figs. 7d and 8d,h). The larger initial distance between the CL and the TC helps maintain the CL structure. As a result, the meridional component of upper-tropospheric steering flow stays around 1 m s^{-1} during $T = 0$–72 h (Fig. 8h).

d. PV tendency analysis

To examine the contributions of different processes to TC motion, the PV tendency method is applied (see section 3c). Figure 9 shows the distribution of wavenumber-1 PVT, HAD, VAD, and DHT during the periods before and after the sudden track change of TCs in NW_In_Deep and NW_Out_Deep experiments. As expected, the orientations of PVT terms vary with time, and the direction of TC motion points to the region of maximum PVT. The pattern of HAD is similar to PVT, indicating a dominant contribution of HAD to the PVT in both simulations. In NW_In_Deep, the maximum positive HAD is to the southwest of the TC center at $T = 12$ h, indicating a southward movement. Thereafter, the location of maximum positive HAD rotated by nearly 180° counterclockwise between $T = 12$–42 h. Both VAD and DHT are small and their effect on TC motion is thus minimal (Figs. 9c,d,g,h). In contrast, the maximum positive HAD in NW_Out_Deep is much weaker, which is consistent with the slower TC motion. The maximum DHT exhibits a direction approximately 90° away from that of the HAD, thereby influencing the pattern of PVT at $T = 33$ h. In both NW_In_Deep and NW_Out_Deep, each term that contributes to PVT intensifies after the TC experiences a

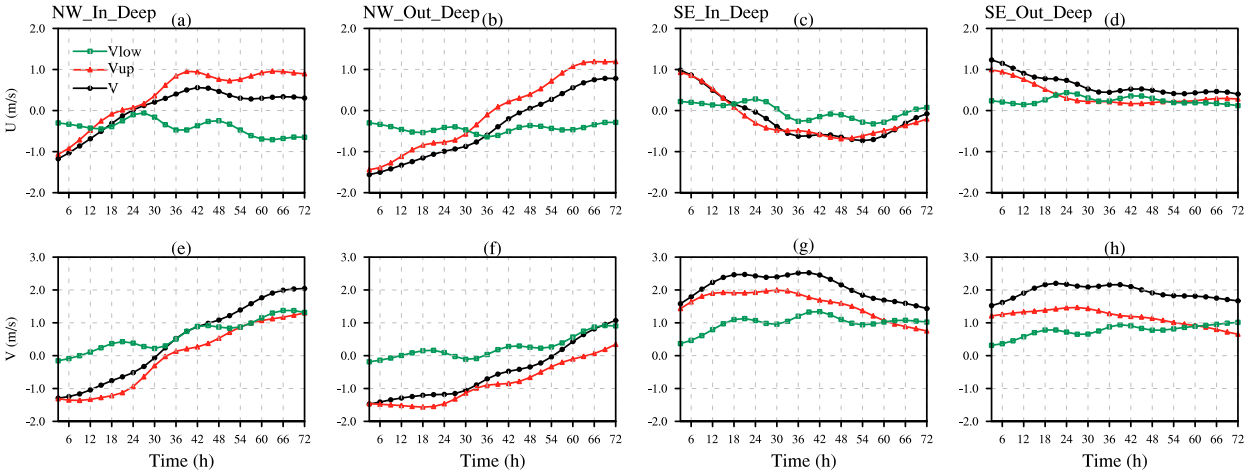

FIG. 8. Evolutions of the (top) zonal and (bottom) meridional components of the steering flow averaged within different heights in (a),(e) NW_In_Deep; (b),(f) NW_Out_Deep; (c),(g) SE_In_Deep; and (d),(h) SE_Out_Deep. The black line with circles is the total steering flow (bottom of Fig. 7), the red line with triangles is the height-averaged steering flow above 550 hPa, and the green line with squares is the height-averaged steering flow below 550 hPa.

sudden northward turn. The maximum HAD shifts from the west flank of TC to the northeast flank during T = 33–72 h. The angle between maximum DHT and HAD decreases by T = 72 h, and the contribution of DHT to the overall PVT distribution diminishes due to the increase of HAD. The contribution of VAD remains insignificant in the NW_Out_Deep.

For the "SE" experiments (Fig. 10), the maximum positive HAD is located in the north (northeast) quadrant of the TC in SE_In_Deep (SE_Out_Deep) at T = 12 h. The maximum HAD in SE_In_Deep then rotates roughly 90° counterclockwise and is situated to the west of the TC center by T = 72 h. The maximum values for VAD and DHT are 1.5×10^{-5} and 12×10^{-5} PVU s^{-1}, respectively (1 PVU = 10^{-6} K kg^{-1} m^2 s^{-1}), indicating their smaller contributions to the total PVT distribution in SE_In_Deep. Nevertheless, the HAD in SE_Out_Deep rotates more slowly due to the persistence of the CL. The location of the maximum HAD correlates well with the direction of steering flow in all simulations (Figs. 9b,f,j,n and 10b,f,j,n). The DHT and VAD terms have minor contributions to the distribution of PVT at T = 72 h.

In short, the HAD term plays the dominant role in the PVT tendency in all simulations. Physically, the changes of HAD can be attributed to two factors [Eq. (7)]: the horizontal gradient of PV and the asymmetric flow across the TC center. First, the CL provides a positive PV anomaly (or, gradient) for the TC in the upper level, in the early stage. The interaction between CL and TC redistributes the PV field, leading to a modification of the PV gradient near the TC and consequently altering the HAD. Second, since the location of the maximum HAD largely coincides with the direction of the steering flow (Figs. 9b,f,j,n and 10b,f,j,n), the HAD pattern is mainly related to the asymmetric flow across the TC center. The above results motivate us to investigate the possible processes accounting for the asymmetric HAD.

e. *Lower-tropospheric circulation*

Figure 11 shows the evolution of the wavenumber-1 pattern of the 700-hPa wind fields, which consists of a cyclonic gyre and an anticyclonic gyre. In addition to the β effect, the CL also contributes to the development of the wavenumber-1 asymmetry. The initial orientation of the wavenumber-1 pattern is strongly influenced by the relative position of the CL and the TC. The cyclonic gyre typically appeared southeast or south of the TC center in the NW experiments and appeared northwest of the TC in the SE experiments (Figs. 11a,e,i,m), and the gyre couplet rotates counterclockwise. With the weakening of the CL circulation at the later stage, the contribution of the β effect increases, and the associated ventilation flow becomes dominant in steering the TC. The ventilation flow refers to the asymmetric flow over the TC core region between a pair of counterrotating asymmetric gyres (the β gyres; Fiorino and Elsberry 1989).

It is worth noting that the HAD maxima are largely located between the gyre couplet, suggesting that the advection of the wavenumber-1 PV by the azimuthal mean tangential flow plays a dominant role in the wavenumber-1 HAD. The ventilation flow is thus generally consistent with the HAD distribution, pointing from negative HAD to positive HAD and consistent with the TC motion vector (Figs. 9–11).

In NW_Out_Deep, the CL can be maintained longer due to the larger distance between the CL and the TC (Fig. 3b). The superposition of the CL and the TC circulations generates an asymmetric flow similar to the one in NW_In_Deep during T = 12–33 h (Figs. 11a,f). Due to the merging of the two systems, the asymmetric flow associated with the CL diminishes and the scale of the TC increases, thereby enhancing the β gyres (Figs. 4 and 11a–d,f–h). In NW_In_Deep, the faster merging of TC and CL results in faster development of β gyres than in NW_Out_Deep (Figs. 11d,h).

In SE_In_Deep, the small initial separation distance between CL and TC enables a partial merging of the two systems, resulting

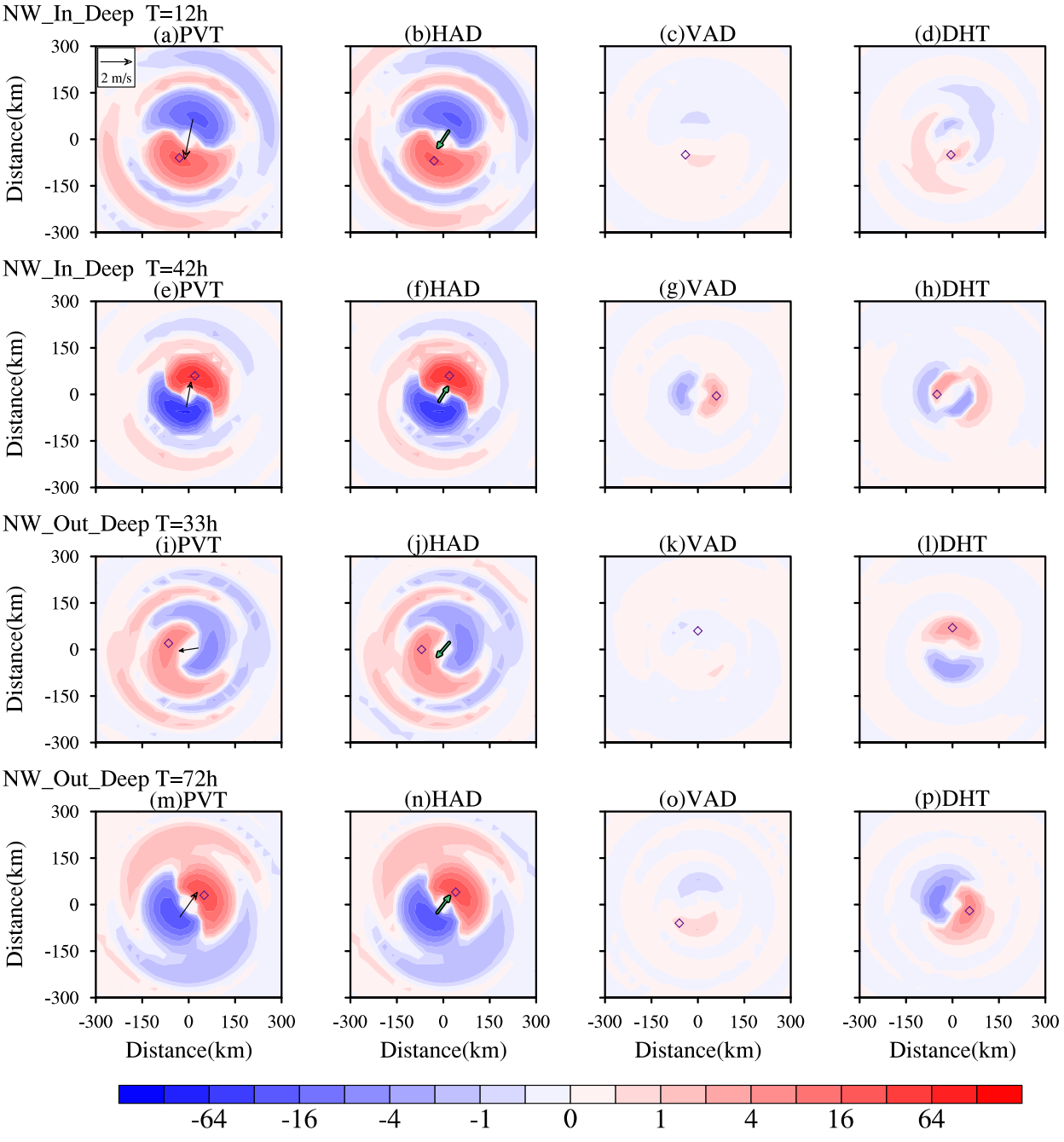

FIG. 9. The wavenumber-1 component of total PV tendency (PVT), horizontal advection (HAD), vertical advection (VAD), and diabatic heating (DHT) terms (units: 10^{-5} PVU s^{-1}) (a)–(d) at T = 12 h and (e)–(h) at T = 42 h in NW_In_Deep; (i)–(l) at T = 33 h, and (m)–(p) at T = 72 h in NW_Out_Deep. These terms are averaged over 850–350 hPa. The black vector indicates the direction of TC motion, the green vector indicates the direction of steering flow, and (0, 0) is the center of the TC. The purple diamond represents the location of the maximum value for each term.

in the enhancement of asymmetry (Figs. 5a–c). Since the CL is located on the northwest flank of the TC, the meridional component of the asymmetric flow induced by CL aligns with that of the ventilation flow brought by β gyres. This alignment strengthens the southerly asymmetric flow across the TC (Figs. 11i–k). After T = 42 h, the circulation of CL dissipates, and the ventilation of β gyres dominates the TC motion (Fig. 11l). In SE_Out_Deep, the asymmetric flow depends more on the strength of the CL because the CL and TC remain far apart until T = 72 h (Fig. 3h), even though β gyres also evolve. In summary, due to the longer persistence of the CL, the asymmetric flow across the TC is more pronounced in the

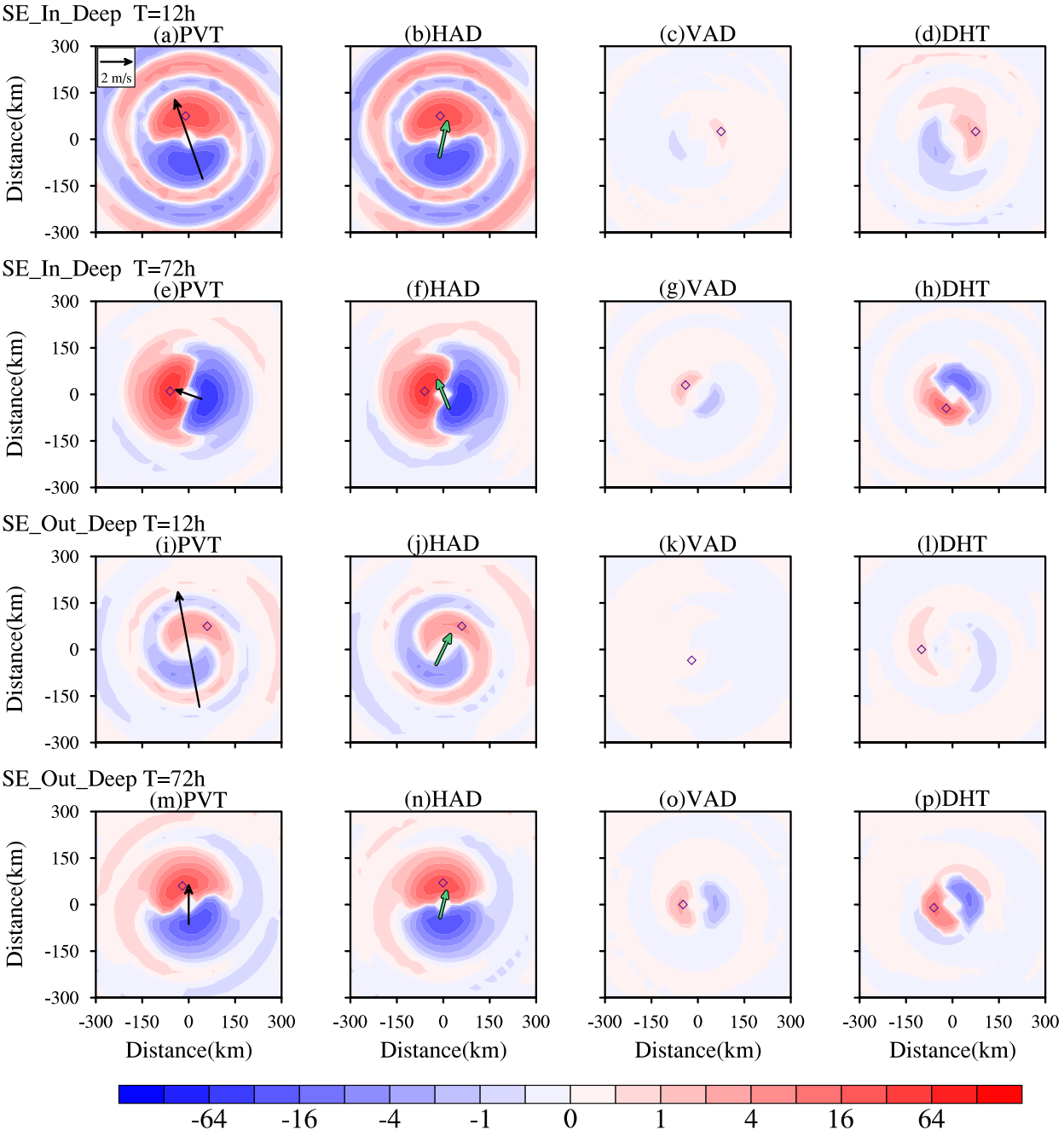

FIG. 10. As in Fig. 9, but for (a)–(h) SE_In_Deep at (a)–(d) T = 12 h and (e)–(h) T = 72 h and for (i)–(p) SE_Out_Deep at (i)–(l) T = 12 h and (m)–(p) T = 72 h.

"SE_Deep" experiments than in the "NW_Deep" experiments. Meanwhile, as the asymmetric flow induced by CL decreases with height, the contribution of ventilation flow brought by β gyres will quickly dominate in all simulations.

5. TC influenced by CL with different depths

In this section, we examine the sensitivity of the TC motion to the CL depth. Figure 12 shows the simulated TC tracks from T = 0–72 h with "Deep," "Medium," and "Shallow" CLs (Table 1). The TC track in the absence of a CL is also shown in Fig. 12b (black line) for comparison. For the "NW" experiments, the TC tracks in the "Medium" and "Shallow" experiments are similar and different from the "Deep" experiment (Fig. 12a). In both NW_In_Medium and NW_In_Shallow, the TCs primarily move westward slowly during T = 0–33 h and shifted to northwestward The TC tracks in NW_Out_Medium and NW_Out_Shallow move mainly westward at early stage and

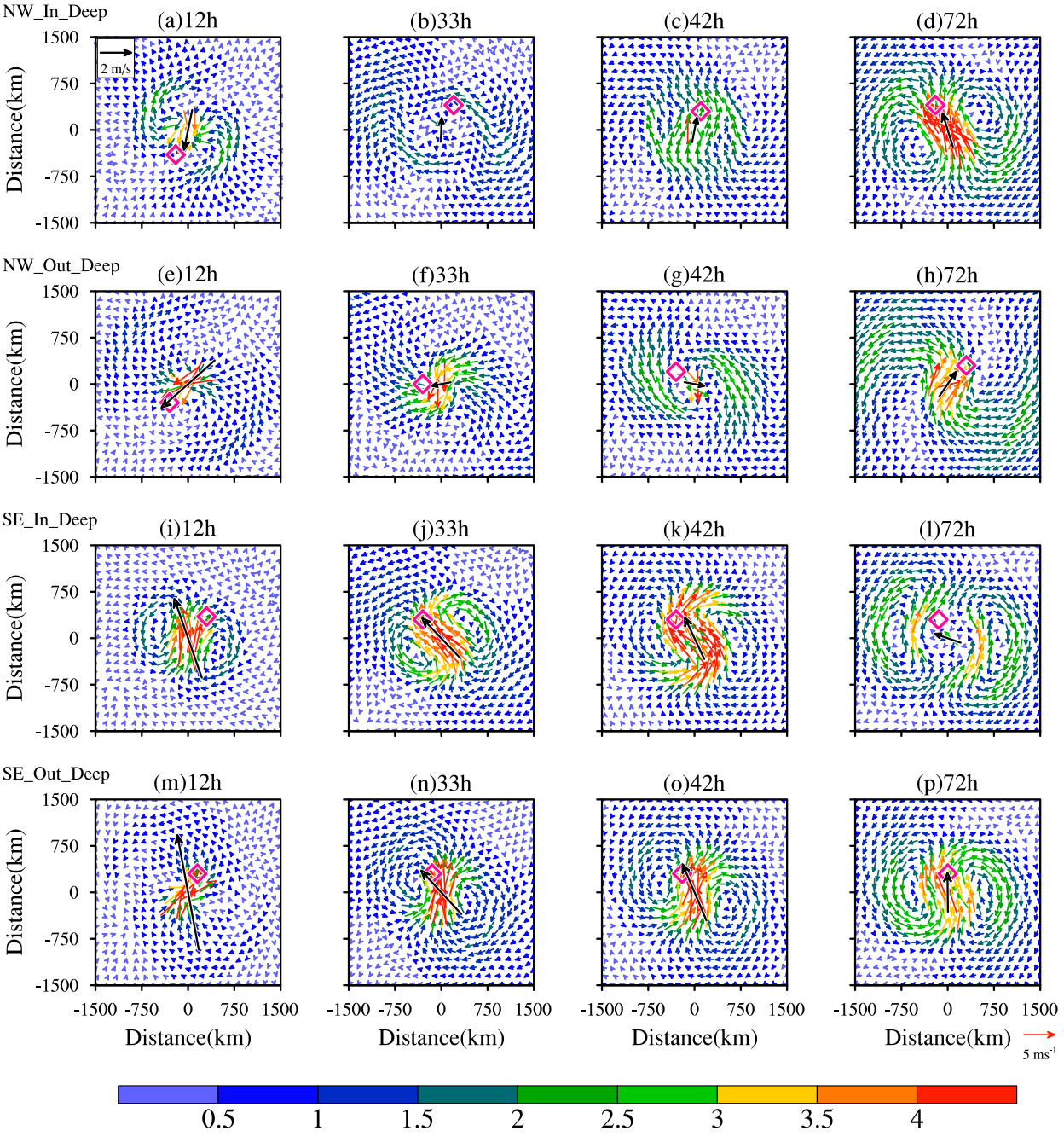

FIG. 11. Evolutions of the simulated wavenumber-1 700-hPa asymmetric wind field (vectors; unit: m s^{-1}) in the (a)–(d) NW_In_Deep, (e)–(h) NW_Out_Deep, (i)–(l) SE_In_Deep, and (m)–(p) SE_Out_Deep. The black vector indicates the direction of TC motion, and (0, 0) is the center of the TC. The pink diamond represents the direction of maximum positive HAD.

then turn northwestward at different times (Fig. 12a). The major difference from the different depth of CL is that circulation of a deep CL controls the TC motion to move southward in early stage while circulation of a shallower CL combines with the β steering to cause a westward TC motion. Furthermore, with a shallower CL, the TC and CL have less interaction and the CL persists longer even when the TC is resided within the CL.

The TC undergoes a smooth cyclonic or north-by-northwest track for all depths of the CL in "SE_In" experiments (Fig. 12b). In contrast, in the absence of background flow, the TC in noCL moves slowly northwestward due to the β effect. In SE_Out_Medium and SE_Out_Shallow, the TCs primarily move northward during T = 0–33 h and the "Medium" CL makes the TC track more northward. After

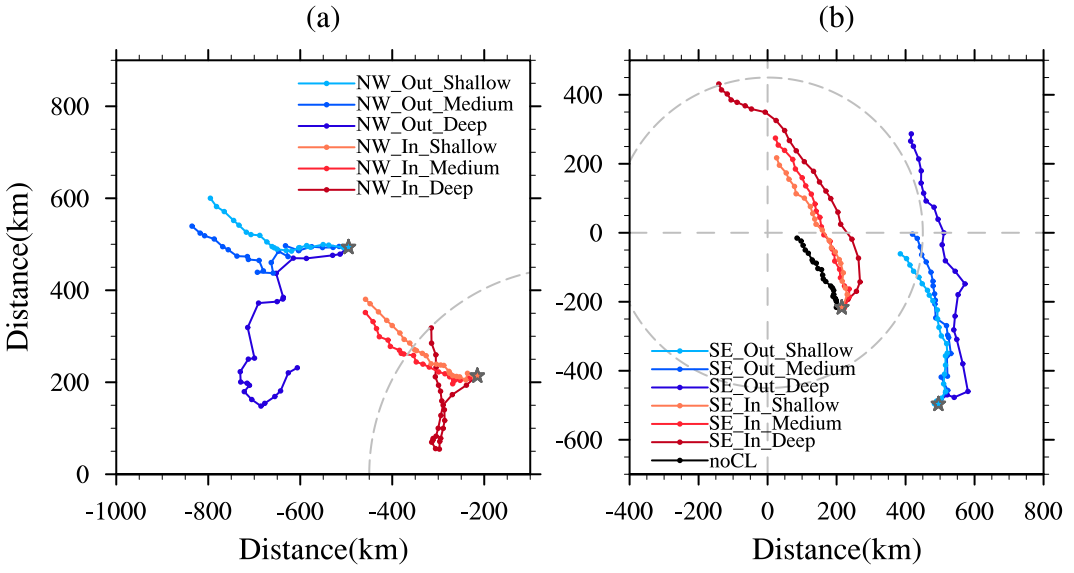

FIG. 12. Simulated 3-hourly tracks of the TC relative to the initial CL center in (a) NW experiments and (b) SE experiments with different depths of CL (Fig. 2b) and noCL experiment. The gray star symbols indicate the positions of the initial TC, and the gray dashed circle represents the RMW of the initial CL. The point (0, 0) is the initial location of CL.

T = 48 h, the translation speed of TCs in both experiments slowed and shifted to move northwestward (Fig. 12b). Among the three different CLs, the deeper the CL, the stronger influence it exerts on the TC through its steering flow, resulting in a longer counterclockwise track.

Figure 13 presents the evolutions of the upper-tropospheric steering flow, lower-tropospheric steering flow, and the total steering flow in the "NW_Medium" and "NW_Shallow" experiments. Combined with Fig. 8, the upper-tropospheric steering flows in NW experiments all experience a transition from the northeasterly to the southwesterly flow (Figs. 8a,b,e,f and 13). Due to the different wind profiles of the CL (Fig. 2b), the initial upper-tropospheric steering flows in the "Shallow" and "Medium" experiments are accordingly reduced by nearly half and one-quarter compared to those in the "Deep" experiments (Figs. 8 and 13). As a result, the developing southerly lower-tropospheric steering flows can counteract the northeasterly upper-tropospheric steering flows, leading to the westward movement of TCs during T = 0–30 h in the "NW_Medium" and "NW_Shallow" experiments (Figs. 13e–h). After T = 30 h, as the β gyres develop, the zonal components of the upper- and low-tropospheric steering flow offset, while the meridional components are in the same direction, leading to enhanced northwestward movement of TCs. These scenarios resemble the "NW_Deep" experiments. In contrast, the upper-tropospheric steering flows are weaker, resulting in a dominant contribution of the β effect to the TC motion in the later stage. Overall, the steering flows in the "NW_Medium" and

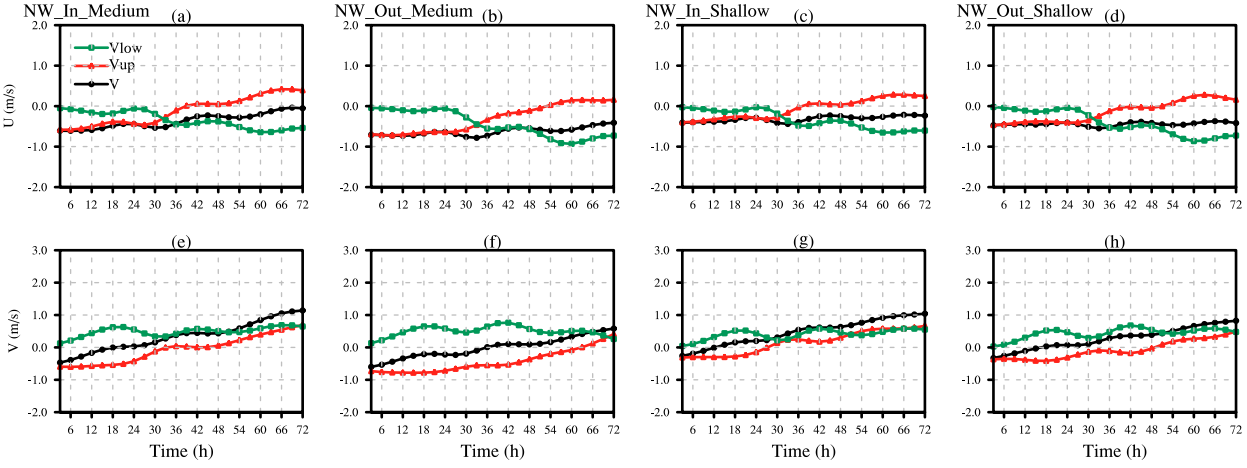

FIG. 13. As in Fig. 8, but for (a),(e) NW_In_Medium; (b),(f) NW_Out_Medium; (c),(g) NW_In_Shallow; and (d),(h) NW_Out_Shallow.

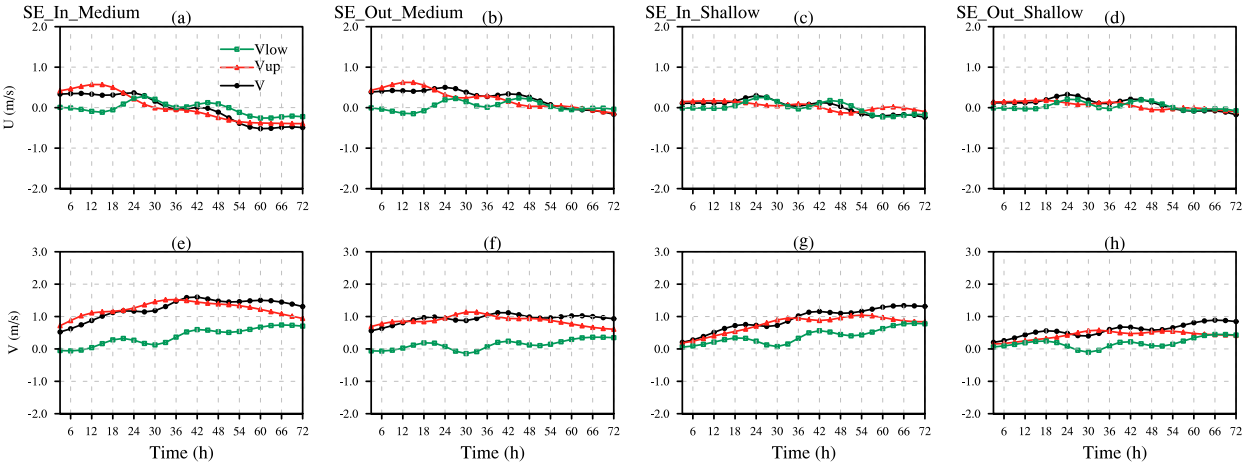

FIG. 14. As in Fig. 8, but for (a),(e) SE_In_Medium; (b),(f) SE_Out_Medium; (c),(g) SE_In_Shallow; and (d),(h) SE_Out_Shallow.

"NW_Shallow" are very similar (Fig. 13), likely resulting in a similar TC track in these four experiments irrespective of their relative distances to the CL.

Figure 14 compares the evolutions of total steering flow, upper- and lower-tropospheric steering flow in the "SE_Medium" and "SE_Shallow" experiments. Despite differences in the initial CL depth, the evolutions of the steering flow show remarkable similarities across all "SE" experiments (Figs. 8c,d,g,h and 14), resulting in similar TC tracks (Fig. 12b). Compared to the "Deep" experiments, the meridional components of the lower-tropospheric steering flows in the "Medium" and "Shallow" experiments are approximately half at later stage (Figs. 8e–h, 13e–h, and 14e–h). This reduction in magnitude is attributed to the weaker β gyres. In the "Deep" experiments, the stronger TC–CL interaction results in stronger β gyres, which contribute to meridional components of the lower-tropospheric steering flow reaching or even exceeding 1 m s^{-1} (Figs. 8e–h). As a result, the TC exhibits faster movement in the "Deep" experiments.

6. Discussion and conclusions

TCs under the influence of an upper-tropospheric cold low (CL) can develop unusual tracks, such as Typhoon Jongdari (2018) and Typhoon Ken-Lola (1989). In this study, idealized simulations are conducted to investigate the TC–CL interactions and how TC tracks vary with the initial position of the TC relative to the CL and with different depths of the CL. A TC initially located east of CL moves northward/northwestward following a smooth counterclockwise semicircle track around the CL, a combined effect of the CL steering and the β effect (Figs. 3c,d). In contrast, a TC initially located west of CL is steered south and southwestward by the CL in the early stage. When the TC is close to the CL, the CL approaches the TC quickly with the TC moving southward and the CL moving northward. With a deep CL, TC–CL interactions are strong enough to erode the CL so that its steering effect on TC weakens and the TC experiences a small looping track from moving southward under CL steering in the early stage to moving northward under β steering at the later stage (Figs. 3a,b).

The upper-tropospheric flow from the CL contributes more to the TC motion in all simulations at the early stage. At the later stage, the divergent outflow of TC erodes the CL circulation as the CL approaches the TC (Figs. 3 and 6). The contribution of upper-tropospheric steering flow thus diminishes while that of the lower-tropospheric steering flow increases (Figs. 7 and 8). This transition plays a key role in the changes of TC's movement direction, especially the stagnation points when the TC is located west of the CL. The PV tendency diagnosis shows that the horizontal advection (HAD) is the primary contributor to the TC motion (Figs. 9 and 10). The different spatial patterns of HAD terms are mainly attributed to the asymmetric flow across the TC center, which is influenced by the CL. The CL circulation can induce the cyclonic asymmetric gyres near the TC, resulting in a different asymmetric flow pattern based on the position of CL at early stage. As the complete/partial merging of CL and TC, the TC scale increases (Fig. 4), and the asymmetric flow consists of the asymmetric flow induced by the CL and the β gyres. After the CL's circulation breaks down or merges with the TC (Figs. 4 and 5), the contribution of the lower-tropospheric asymmetric flow due to the β gyres becomes dominant in most of the experiments (Fig. 11).

The separation distance between CL and TC is a critical factor in determining the TC–CL interaction and the TC motion through the strength of the steering flow. When the TC is initially located within the radius of maximum wind (RMW) of the CL, the stronger TC–CL interaction leads to a change in TC track in the "NW" cases. In contrast, for the "SE" cases, the TC follows a counterclockwise semicircle track, irrespective of the separation distance. The main reason is that the steering from the CL is opposing the β steering when the TC is on the west side, and they are more parallel when the TC is on the east side of CL.

The sensitivity of the TC track to the depth of the CL is also examined. In the "NW" experiments, a shallower CL leads to a more zonal TC track at the early stage, followed by

more northwestward motion (Fig. 12a). If the TC is located east of a CL, the CL depth mainly affects the speed of the TC motion and the curvature of the cyclonic track (Fig. 12b). The TC exhibits faster movement in the "Deep" experiments. As the influence of the upper-tropospheric steering flow diminishes with the decrease of the CL depth, the contribution of lower-tropospheric steering flow induced by the β gyres increases.

In summary, our idealized simulations explain well different behaviors of TC tracks in the presence of a nearby CL in real cases. The TC–CL interaction is also expected to affect the TC intensity evolution. A thorough investigation of TC intensity evolution in these experiments is underway and will be reported in a separate paper.

Acknowledgments. We acknowledge three anonymous reviewers for their valuable comments that help improve the quality of this manuscript. This work was jointly sponsored by the National Natural Science Foundation of China (42088101; 42175003; U2342202; 42175008) and the Open Grants of the State Key Laboratory of Severe Weather (2022LASW-B08). ZW is supported by the National Science Foundation of the United States (2116804). The numerical calculations in this paper have been done in the Supercomputing Center of Nanjing University of Information Science and Technology.

Data availability statement. The datasets that are either or both generated and analyzed in this study are available from the corresponding author on reasonable request.

REFERENCES

Bi, M., T. Li, M. Peng, and X. Shen, 2015: Interactions between Typhoon Megi (2010) and a low-frequency monsoon gyre. *J. Atmos. Sci.*, **72**, 2682–2702, https://doi.org/10.1175/JAS-D-14-0269.1.

Camargo, S. J., A. W. Robertson, S. J. Gaffney, P. Smyth, and M. Ghil, 2007: Cluster analysis of typhoon tracks. Part I: General properties. *J. Climate*, **20**, 3635–3653, https://doi.org/10.1175/JCLI4188.1.

Carr, L. E., III, and R. L. Elsberry, 1995: Monsoonal interactions leading to sudden tropical cyclone track changes. *Mon. Wea. Rev.*, **123**, 265–290, https://doi.org/10.1175/1520-0493(1995)123<0265:MILTST>2.0.CO;2.

——, and ——, 1998: Objective diagnosis of binary tropical cyclone interactions for the western North Pacific basin. *Mon. Wea. Rev.*, **126**, 1734–1740, https://doi.org/10.1175/1520-0493(1998)126<1734:ODOBTC>2.0.CO;2.

Chan, J. C. L., and W. M. Gray, 1982: Tropical cyclone movement and surrounding flow relationships. *Mon. Wea. Rev.*, **110**, 1354–1374, https://doi.org/10.1175/1520-0493(1982)110<1354:TCMASF>2.0.CO;2.

——, F. M. F. Ko, and Y. M. Lei, 2002: Relationship between potential vorticity tendency and tropical cyclone motion. *J. Atmos. Sci.*, **59**, 1317–1336, https://doi.org/10.1175/1520-0469(2002)059<1317:RBPVTA>2.0.CO;2.

Chen, G. T.-J., and L.-F. Chou, 1994: An investigation of cold vortices in the upper troposphere over the western North Pacific during the warm season. *Mon. Wea. Rev.*, **122**, 1436–1448, https://doi.org/10.1175/1520-0493(1994)122<1436:AIOCVI>2.0.CO;2.

Chen, L., and Y. Ding, 1979: *An Introduction to the Western Pacific Typhoons* (in Chinese). Science Press, 491 pp.

——, X. Xu, Z. Luo, and J. Wang, 2002: *Introduction to Tropical Cyclone Dynamics* (in Chinese). Meteorology Press, 317 pp.

Dritschel, D. G., and D. W. Waugh, 1992: Quantification of the inelastic interaction of unequal vortices in two-dimensional vortex dynamics. *Phys. Fluids*, **4A**, 1737–1744, https://doi.org/10.1063/1.858394.

Dudhia, J., 1989: Numerical study of convection observed during the winter monsoon experiment using a mesoscale two-dimensional model. *J. Atmos. Sci.*, **46**, 3077–3107, https://doi.org/10.1175/1520-0469(1989)046<3077:NSOCOD>2.0.CO;2.

Fiorino, M., and R. L. Elsberry, 1989: Some aspects of vortex structure related to tropical cyclone motion. *J. Atmos. Sci.*, **46**, 975–990, https://doi.org/10.1175/1520-0469(1989)046<0975:SAOVSR>2.0.CO;2.

Galarneau, T. J., Jr., and C. A. Davis, 2013: Diagnosing forecast errors in tropical cyclone motion. *Mon. Wea. Rev.*, **141**, 405–430, https://doi.org/10.1175/MWR-D-12-00071.1.

Ge, X., Z. Yan, M. Peng, M. Bi, and T. Li, 2018: Sensitivity of tropical cyclone track to the vertical structure of a nearby monsoon gyre. *J. Atmos. Sci.*, **75**, 2017–2028, https://doi.org/10.1175/JAS-D-17-0201.1.

Hanley, D., J. Molinari, and D. Keyser, 2001: A composite study of the interactions between tropical cyclones and upper-tropospheric troughs. *Mon. Wea. Rev.*, **129**, 2570–2584, https://doi.org/10.1175/1520-0493(2001)129<2570:ACSOTI>2.0.CO;2.

Harr, P. A., and R. L. Elsberry, 1991: Tropical cyclone track characteristics as a function of large-scale circulation anomalies. *Mon. Wea. Rev.*, **119**, 1448–1468, https://doi.org/10.1175/1520-0493(1991)119<1448:TCTCAA>2.0.CO;2.

——, and ——, 1995: Large-scale circulation variability over the tropical western North Pacific. Part I: Spatial patterns and tropical cyclone characteristics. *Mon. Wea. Rev.*, **123**, 1225–1246, https://doi.org/10.1175/1520-0493(1995)123<1225:LSCVOT>2.0.CO;2.

Hersbach, H., and Coauthors, 2020: The ERA5 global reanalysis. *Quart. J. Roy. Meteor. Soc.*, **146**, 1999–2049, https://doi.org/10.1002/qj.3803.

Holland, G. J., 1983: Tropical cyclone motion: Environmental interaction plus a beta effect. *J. Atmos. Sci.*, **40**, 328–342, https://doi.org/10.1175/1520-0469(1983)040<0328:TCMEIP>2.0.CO;2.

Hong, S.-Y., Y. Noh, and J. Dudhia, 2006: A new vertical diffusion package with an explicit treatment of entrainment processes. *Mon. Wea. Rev.*, **134**, 2318–2341, https://doi.org/10.1175/MWR3199.1.

——, K.-S. S. Lim, Y.-H. Lee, J.-C. Ha, H.-W. Kim, S.-J. Ham, and J. Dudhia, 2010: Evaluation of the WRF double-moment 6-class microphysics scheme for precipitating convection. *Adv. Meteor.*, **2010**, 707253, https://doi.org/10.1155/2010/707253.

Huang, Q., X. Ge, and M. Bi, 2022: Simulation of rapid intensification of super Typhoon Lekima (2019). Part II: The critical role of cloud-radiation interaction of asymmetric convection. *Front. Earth Sci.*, **9**, 832670, https://doi.org/10.3389/feart.2021.832670.

Ito, K., C.-C. Wu, K. T. F. Chan, R. Toumi, and C. Davis, 2020: Recent progress in the fundamental understanding of tropical cyclone motion. *J. Meteor. Soc. Japan*, **98**, 5–17, https://doi.org/10.2151/jmsj.2020-001.

Jiménez, P. A., J. Dudhia, J. F. González-Rouco, J. Navarro, J. P. Montávez, and E. García-Bustamante, 2012: A revised scheme for the WRF surface layer formulation. *Mon. Wea. Rev.*, **140**, 898–918, https://doi.org/10.1175/MWR-D-11-00056.1.

Jordan, C. L., 1958: Mean soundings for the West Indies area. *J. Meteor.*, **15**, 91–97, https://doi.org/10.1175/1520-0469(1958)015<0091:MSFTWI>2.0.CO;2.

Kain, J. S., and J. M. Fritsch, 1993: Convective parameterization for mesoscale models: The Kain–Fritsch scheme. *The Representation of Cumulus Convection in Numerical Models*, *Meteor. Monogr.*, No. 46, Amer. Meteor. Soc., 165–170, https://doi.org/10.1007/978-1-935704-13-3_16.

Kelley, W. E., Jr., and D. R. Mock, 1982: A diagnostic study of upper tropospheric cold lows over the western North Pacific. *Mon. Wea. Rev.*, **110**, 471–480, https://doi.org/10.1175/1520-0493(1982)110<0471:ADSOUT>2.0.CO;2.

Khain, A., I. Ginis, A. Falkovich, and M. Frumin, 2000: Interaction of binary tropical cyclones in a coupled tropical cyclone-ocean model. *J. Geophys. Res.*, **105**, 22 337–22 354, https://doi.org/10.1029/2000JD900268.

Knapp, K. R., M. C. Kruk, D. H. Levinson, H. J. Diamond, and C. J. Neumann, 2010: The International Best Track Archive for Climate Stewardship (IBTrACS): Unifying tropical cyclone data. *Bull. Amer. Meteor. Soc.*, **91**, 363–376, https://doi.org/10.1175/2009BAMS2755.1.

——, H. J. Diamond, J. P. Kossin, M. C. Kruk, and C. J. Schreck, 2018: International Best Track Archive for Climate Stewardship (IBTrACS) project, version 4. NOAA/National Centers for Environmental Information, accessed 30 July 2021, https://doi.org/10.25921/82ty-9e16.

Kuo, H.-C., L.-Y. Lin, C.-P. Chang, and R. T. Williams, 2004: The formation of concentric vorticity structures in typhoons. *J. Atmos. Sci.*, **61**, 2722–2734, https://doi.org/10.1175/JAS3286.1.

Lander, M. A., 1996: Specific tropical cyclone track types and unusual tropical cyclone motions associated with a reverse-oriented monsoon trough in the western North Pacific. *Wea. Forecasting*, **11**, 170–186, https://doi.org/10.1175/1520-0434(1996)011<0170:STCTTA>2.0.CO;2.

——, and G. J. Holland, 1993: On the interaction of tropical-cyclone-scale vortices. I: Observations. *Quart. J. Roy. Meteor. Soc.*, **119**, 1347–1361, https://doi.org/10.1002/qj.49711951406.

Lei, L., Y. Ge, Z. Tan, and X. Bao, 2020: An evaluation and improvement of tropical cyclone prediction in the western North Pacific basin from global ensemble forecasts. *Sci. China Earth Sci.*, **63**, 12–26, https://doi.org/10.1007/s11430-019-9480-8.

Li, Y., L.-X. Guo, Y.-L. Xu, and S. Hu, 2012: Impacts of upper-level cold vortex on the rapid change of intensity and motion of Typhoon Meranti (2010). *J. Trop. Meteor.*, **18**, 207–219.

Liang, J., and L. Wu, 2015: Sudden track changes of tropical cyclones in monsoon gyres: Full-physics, idealized numerical experiments. *J. Atmos. Sci.*, **72**, 1307–1322, https://doi.org/10.1175/JAS-D-13-0393.1.

Liou, Y.-A., and R. S. Pandey, 2020: Interactions between Typhoons Parma and Melor (2009) in North West Pacific Ocean. *Wea. Climate Extremes*, **29**, 100272, https://doi.org/10.1016/j.wace.2020.100272.

Mlawer, E. J., S. J. Taubman, P. D. Brown, M. J. Iacono, and S. A. Clough, 1997: Radiative transfer for inhomogeneous atmospheres: RRTM, a validated correlated-k model for the longwave. *J. Geophys. Res.*, **102**, 16 663–16 682, https://doi.org/10.1029/97JD00237.

Molinari, J., and D. Vollaro, 1989: External influences on hurricane intensity. Part I: Outflow layer eddy angular momentum fluxes. *J. Atmos. Sci.*, **46**, 1093–1105, https://doi.org/10.1175/1520-0469(1989)046<1093:EIOHIP>2.0.CO;2.

Palmén, E., 1949: Origin and structure of high-level cyclones south of the maximum westerlies. *Tellus*, **1**, 22–31, https://doi.org/10.1111/j.2153-3490.1949.tb01925.x.

Palmer, C. E., 1953: The impulsive generation of certain changes in the tropospheric circulation. *J. Meteor.*, **10**d, 1–9, https://doi.org/10.1175/1520-0469(1953)010<0001:TIGOCC>2.0.CO;2.

Patla, J. E., D. Stevens, and G. M. Barnes, 2009: A conceptual model for the influence of TUTT cells on tropical cyclone motion in the northwest Pacific Ocean. *Wea. Forecasting*, **24**, 1215–1235, https://doi.org/10.1175/2009WAF2222181.1.

Postel, G. A., and M. H. Hitchman, 1999: A climatology of Rossby wave breaking along the subtropical tropopause. *J. Atmos. Sci.*, **56**, 359–373, https://doi.org/10.1175/1520-0469(1999)056<0359:ACORWB>2.0.CO;2.

Qian, C., Y. Duan, S. Ma, and Y. Xu, 2012: The current status and future development of China operational typhoon forecasting and its key technologies (in Chinese). *Adv. Meteor. Sci. Technol.*, **2**, 36–43.

——, F. Zhang, B. W. Green, J. Zhang, and X. Zhou, 2013: Probabilistic evaluation of the dynamics and prediction of Supertyphoon Megi (2010). *Wea. Forecasting*, **28**, 1562–1577, https://doi.org/10.1175/WAF-D-12-00121.1.

Ryglicki, D. R., J. D. Doyle, D. Hodyss, J. H. Cossuth, Y. Jin, K. C. Viner, and J. M. Schmidt, 2019: The unexpected rapid intensification of tropical cyclones in moderate vertical wind shear. Part III: Outflow–environment interaction. *Mon. Wea. Rev.*, **147**, 2919–2940, https://doi.org/10.1175/MWR-D-18-0370.1.

Sadler, J. C., 1975: The monsoon circulation and cloudiness over the GATE area. *Mon. Wea. Rev.*, **103**, 369–387, https://doi.org/10.1175/1520-0493(1975)103<0369:TMCACO>2.0.CO;2.

——, 1976: A role of the tropical upper tropospheric trough in early season typhoon development. *Mon. Wea. Rev.*, **104**, 1266–1278, https://doi.org/10.1175/1520-0493(1976)104<1266:AROTTU>2.0.CO;2.

Shapiro, L. J., 1996: The motion of Hurricane Gloria: A potential vorticity diagnosis. *Mon. Wea. Rev.*, **124**, 2497–2508, https://doi.org/10.1175/1520-0493(1996)124<2497:TMOHGA>2.0.CO;2.

——, and J. L. Franklin, 1995: Potential vorticity in Hurricane Gloria. *Mon. Wea. Rev.*, **123**, 1465–1475, https://doi.org/10.1175/1520-0493(1995)123<1465:PVIHG>2.0.CO;2.

——, and ——, 1999: Potential vorticity asymmetries and tropical cyclone motion. *Mon. Wea. Rev.*, **127**, 124–131, https://doi.org/10.1175/1520-0493(1999)127<0124:PVAATC>2.0.CO;2.

Skamarock, W. C., and Coauthors, 2008: A description of the Advanced Research WRF version 3. NCAR Tech. Note NCAR/TN-475+STR, 113 pp., https://doi.org/10.5065/D68S4MVH.

Velden, C. S., and L. M. Leslie, 1991: The basic relationship between tropical cyclone intensity and the depth of the environmental steering layer in the Australian region. *Wea. Forecasting*, **6**, 244–253, https://doi.org/10.1175/1520-0434(1991)006<0244:TBRBTC>2.0.CO;2.

Wang, M. Y.-M., G. T.-J. Chen, C.-C. Wang, and Y.-H. Kuo, 2012: A case study of the cutoff process and latent heating effect in an upper-level cold-core low during the mei-yu season in East Asia. *Mon. Wea. Rev.*, **140**, 1725–1747, https://doi.org/10.1175/MWR-D-11-00306.1.

Wang, X., and D.-L. Zhang, 2003: Potential vorticity diagnosis of a simulated hurricane. Part I: Formulation and quasi-balanced

flow. *J. Atmos. Sci.*, **60**, 1593–1607, https://doi.org/10.1175/2999.1.

Wang, Y., 1995: An inverse balance equation in sigma coordinates for model initialization. *Mon. Wea. Rev.*, **123**, 482–488, https://doi.org/10.1175/1520-0493(1995)123<0482:AIBEIS>2.0.CO;2.

Wei, N., Y. Li, D.-L. Zhang, Z. Mai, and S.-Q. Yang, 2016: A statistical analysis of the relationship between upper-tropospheric cold low and tropical cyclone track and intensity change over the western North Pacific. *Mon. Wea. Rev.*, **144**, 1805–1822, https://doi.org/10.1175/MWR-D-15-0370.1.

Wen, D., Y. Li, D.-L. Zhang, L. Xue, and N. Wei, 2018: A statistical analysis of tropical upper-tropospheric trough cells over the western North Pacific during 2006–15. *J. Appl. Meteor. Climatol.*, **57**, 2469–2483, https://doi.org/10.1175/JAMC-D-18-0003.1.

——, and Coauthors, 2019: An ensemble analysis on abrupt North turning of Typhoon Meranti (1010) under the influence of an upper tropospheric cold low (in Chinese). *Chin. J. Atmos. Sci.*, **43**, 730–740.

Wu, C.-C., and K. A. Emanuel, 1995a: Potential vorticity diagnostics of hurricane movement. Part I: A case study of Hurricane Bob (1991). *Mon. Wea. Rev.*, **123**, 69–92, https://doi.org/10.1175/1520-0493(1995)123<0069:PVDOHM>2.0.CO;2.

——, and ——, 1995b: Potential vorticity diagnostics of hurricane movement. Part II: Tropical Storm Ana (1991) and Hurricane Andrew (1992). *Mon. Wea. Rev.*, **123**, 93–109, https://doi.org/10.1175/1520-0493(1995)123<0093:PVDOHM>2.0.CO;2.

——, and Y. Kurihara, 1996: A numerical study of the feedback mechanisms of hurricane–environment interaction on hurricane movement from the potential vorticity perspective. *J. Atmos. Sci.*, **53**, 2264–2282, https://doi.org/10.1175/1520-0469(1996)053<2264:ANSOTF>2.0.CO;2.

Wu, L., and B. Wang, 2000: A potential vorticity tendency diagnostic approach for tropical cyclone motion. *Mon. Wea. Rev.*, **128**, 1899–1911, https://doi.org/10.1175/1520-0493(2000)128<1899:APVTDA>2.0.CO;2.

——, and ——, 2004: Assessing impacts of global warming on tropical cyclone tracks. *J. Climate*, **17**, 1686–1698, https://doi.org/10.1175/1520-0442(2004)017<1686:AIOGWO>2.0.CO;2.

——, H. Zong, and J. Liang, 2011: Observational analysis of sudden tropical cyclone track changes in the vicinity of the East China Sea. *J. Atmos. Sci.*, **68**, 3012–3031, https://doi.org/10.1175/2010JAS3559.1.

Yan, Z., X. Ge, Z. Wang, C.-C. Wu, and M. Peng, 2021: Understanding the impacts of upper-tropospheric cold low on Typhoon Jongdari (2018) using piecewise potential vorticity inversion. *Mon. Wea. Rev.*, **149**, 1499–1515, https://doi.org/10.1175/MWR-D-20-0271.1.